Gezamenlijke opleiding UHasselt en KU Leuven

Universiteit Hasselt | Campus Diepenbeek | Faculteit Industriële Ingenieurswetenschappen | Agoralaan Gebouw H - Gebouw B | BE 3590 Diepenbeek

Universiteit Hasselt | Campus Diepenbeek | Agoralaan Gebouw D | BE 3590 Diepenbeek
Universiteit Hasselt | Campus Hasselt | Martelarenlaan 42 | BE 3500 Hasselt

---

Faculteit Industriële Ingenieurswetenschappen

master in de industriële wetenschappen: nucleaire technologie

Masterthesis

Preliminary design and evaluation of a 3D-printed phantom for gynecological brachytherapy dosimetry audits

Edward Ketels
Scriptie ingediend tot het behalen van de graad van master in de industriële wetenschappen: nucleaire technologie, afstudeerrichting nucleair en medisch

PROMOTOR :
Prof. dr. Brigitte RENIERS

PROMOTOR :
drs. Roua ABDULRAHIM

COPROMOTOR :
De heer Burak YALVAC

2024
2025

Faculteit Industriële Ingenieurswetenschappen

master in de industriële wetenschappen: nucleaire technologie

Masterthesis

Preliminary design and evaluation of a 3D-printed phantom for gynecological brachytherapy dosimetry audits

Edward Ketels

Scriptie ingediend tot het behalen van de graad van master in de industriële wetenschappen: nucleaire technologie, afstudeerrichting nucleair en medisch

PROMOTOR :

Prof. dr. Brigitte RENIERS

PROMOTOR :

drs. Roua ABDULRAHIM

COPROMOTOR :

De heer Burak YALVAC

Acknowledgements

Presented here is the result of my thesis, a project that marks the final stage of my academic journey. This work could not have been completed without the support, expertise, and dedication of several individuals, to whom I would like to express my sincere gratitude.

First and foremost, I would like to thank Prof. Dr. Brigitte Reniers for sharing her expert knowledge and helping to shape the direction of this research. Her experience and guidance were invaluable to the academic quality of this work.

My special thanks go to Drs. Roua Abdulrahim for her hands-on supervision and her constant availability for questions and discussions. Her involvement and support made a significant difference throughout this process.

I am also grateful to Mr. Burak Yalvac for his assistance with the measurements. His practical support played an important role in the data collection phase.

Furthermore, I would like to thank my parents for giving me the opportunity to pursue this education, and for their unwavering support, trust, and encouragement throughout my studies.

Finally, I would like to sincerely thank Anli for her help in proofreading and finalizing this thesis. Her attention to detail and willingness to contribute greatly enhanced the quality of the final result.

To all of you: thank you for your contribution. Your help, in whatever form, has been deeply meaningful.

Table of Contents

List of Tables

List of Figures

Glossary

3D-CRT	3D conformal radiation therapy
AAPM	American Association of Physicists in Medicine
ABS	American Brachytherapy Society
ART	Adaptive radiotherapy
BT	Brachytherapy
CAD	Computer-aided design
Cesium-137	Cs-137
CT	Computed tomography
EBRT	External beam radiotherapy
EMBRACE	Image guided intensity modulated external beam radiotherapy and magnetic resonance imaging-based adaptive brachytherapy in locally advanced cervical cancer
ESTRO	European Society for Radiotherapy and Oncology
EUA	Examination under anesthesia
FDG	Fluorodeoxyglucose
FDM	Fused deposition modeling
FIGO	International Federation of Gynecology and Obstetrics
HDR-BT	High dose rate brachytherapy
HPV	Human papillomavirus
HR-CTV	High-risk clinical target volume
HU	Hounsfield unit
IGABT	Image-guided adaptive brachytherapy
IMRT	Intensity-modulated radiation therapy
Iridium-192	Ir-192
ISBT	Interstitial brachytherapy
LDR	Low dose rate
MBDCAs	More advanced model-based dose calculation algorithms
MRI	Magnetic resonance imaging
OARs	Organs at risk
OTT	Overall treatment time
PDR	Pulsed dose rate
PET/CT	Positron Emission Tomography-Computed Tomography
PLA	Polylactic acid
PSDs	Plastic scintillator detectors
QA	Quality assurance
RED	Relative electron density
ROI	Region of interest
SLA	Stereolithography
SLS	Selective laser sintering
STL	Stereolithography
TG-43	Task Group 43
TPS	Treatment planning system
TPU	Thermoplastic polyurethane

Abstract

Cervical cancer remains a major cause of cancer-related mortality in low- and middle-income countries, where access to radiotherapy and consistent quality assurance (QA) is limited. High-dose-rate brachytherapy (BT), a key component of curative treatment, demands high geometric accuracy, yet standardized QA tools are often lacking. This thesis presents the development of a reproducible and cost-effective QA phantom for gynecological BT using 3D printing. Commercial BT applicators were reconstructed via computed tomography (CT) and converted into computer-aided design (CAD) models. Test phantoms were fabricated using fused deposition modeling (FDM) with polylactic acid (PLA) for rigid and thermoplastic polyurethane (TPU) for deformable characteristics. Evaluation included dimensional validation, applicator insertion testing, and assessment of CT imaging compatibility. No dimensional deviations exceeded the resolution threshold of the CT imaging system. CT compatibility, structural integrity, and reliability under dosimetric testing were confirmed. These results demonstrate the viability of low-cost 3D printing for QA applications in BT. The developed workflow offers a scalable solution for clinical centres with limited resources and contributes to improved consistency and safety in clinical practice.

Abstract in het Nederlands

Baarmoederhalskanker blijft een belangrijke oorzaak van kankergerelateerde sterfte in lage- en middeninkomenslanden, waar de toegang tot radiotherapie en consistente quality assurance (QA) beperkt is. High-dose-rate brachytherapie (BT), een belangrijk onderdeel van de curatieve behandeling, vereist een hoge geometrische nauwkeurigheid, maar gestandaardiseerde QA-instrumenten ontbreken vaak. Deze masterproef stelt de ontwikkeling, met behulp van 3D-printing, van een reproduceerbaar en kosteneffectief QA-fantoom voor gynaecologische BT voor. Commerciële BT-applicatoren werden gereconstrueerd via computertomografie (CT) en omgezet in Computer Aided Design (CAD)- modellen. Testfantomen werden vervaardigd met behulp van Fused Deposition Modeling (FDM) met polylactide (PLA) voor rigide en thermoplastisch polyurethaan (TPU) voor flexibele karakteristieken. Het model werd geëvalueerd door middel van geometrische analyse, testen met inbrenging van de applicator en beeldcompatibiliteit met CT. Geometrische afwijkingen van het CAD-model bleven kleiner dan de resolutie van de CT. CT-compatibiliteit, structurele integriteit en betrouwbaarheid bij dosimetrische testen werden bevestigd. Deze resultaten tonen de bruikbaarheid aan van goedkoop 3D-printen voor QA-toepassingen in BT. De ontwikkelde workflow biedt een schaalbare oplossing voor klinische centra met beperkte middelen en draagt bij aan verbeterde consistentie en veiligheid in de klinische praktijk.

1. Introduction

Cervical cancer is among the most prevalent malignancies affecting women worldwide, ranking fourth in both incidence and mortality [1], [2]. Despite decades of progress in prevention—particularly through human papillomavirus (HPV) vaccination and screening, the global burden remains high, especially in low- and middle-income countries. In 2020, the WHO estimated 604,000 new cases and 342,000 deaths, highlighting persistent inequities in healthcare access [2],[3].

The disease primarily affects women in their reproductive years, compounding its clinical and socioeconomic impact. Treatment for locally advanced cervical cancer typically involves a multimodal approach combining external beam radiotherapy (EBRT), chemotherapy, and brachytherapy (BT), with each modality addressing systemic, regional, and local disease [4], [5]. EBRT and chemotherapy provide systemic and regional control, while BT enables high-dose localized radiation with rapid falloff [5], [6].

High dose rate BT (HDR-BT) is essential for cervical cancer, especially with complex tumors, but its effectiveness relies on precise geometric accuracy of applicator placement and source positioning. Deviations can cause significant dose alterations due to steep dose gradients [7], [8]. Consequently, robust quality assurance (QA) is imperative, yet standardized BT QA protocols, especially in gynecological contexts, lag behind those for EBRT. Practice variability is increased due to the lack of cost-effective auditing tools, particularly in low-resource settings [9], [10].

To bridge this gap, there is growing interest in QA tools that are adaptable, reproducible, and accessible across diverse clinical environments. 3D printing offers a promising solution, enabling the creation of patient- or application-specific phantoms that replicate anatomical and geometric features, supporting imaging tests, applicator fit, and dosimetry validation, while being affordable and customizable [11], [12].

This thesis presents the development, fabrication, and validation of a 3D-printed phantom for gynecological BT QA using fused deposition modeling (FDM), with polylactic acid (PLA) for rigidity and thermoplastic polyurethane (TPU) for flexibility. Two phantom versions were evaluated in terms of mechanical accuracy, computed tomography (CT) compatibility, applicator insertion behavior, and dosimetric validation via plastic scintillators and radiochromic film.

The goal is to assess whether low-cost, 3D-printed phantoms can serve as standardized QA tools in clinical and training environments, thus addressing the existing infrastructure gap in resource-constrained settings. Additionally, it explores material-dependent trade-offs between structural accuracy and tissue equivalence to guide future phantom designs

2. Literature study

2.1 Literature Search Methodology

The literature reviewed in this chapter was collected through structured searches primarily using PubMed, Google Scholar, and ScienceDirect. Key search terms included: “cervical cancer brachytherapy”, “3D printing radiotherapy QA”, “image-guided adaptive brachytherapy”, “phantom dosimetry”, and “model-based dose calculation algorithms”.
Priority was given to studies published after 2010, with particular emphasis on peer-reviewed clinical research, technical evaluations, and guideline publications from professional bodies such as the American Association of Physicists in Medicine (AAPM) and the European Society for Radiotherapy and Oncology (ESTRO). Reference chaining was used to identify foundational papers cited across multiple reviews.

2.2 Cervical cancer treatment

The standard treatment approach for locally advanced cervical cancer involves a combination of EBRT, chemotherapy, and BT. This multimodal strategy is designed to enhance locoregional control, reduce recurrence, and improve overall survival, particularly in patients with International Federation of Gynecology and Obstetrics (FIGO) stage IB2 and higher [12], [13]. Each modality addresses different aspects of disease management and their integration is essential to achieving curative outcomes [14]. This section outlines the principles and clinical rationale behind each component of therapy, with a particular focus on the evolving role of BT in the context of advanced imaging and precision delivery techniques [15], [16].

2.2.1 External beam radiotherapy

EBRT is integral to the treatment of cervical cancer, particularly for controlling pelvic disease and treating involved lymphatic regions. High-energy photon beams are directed at the tumor and surrounding at-risk structures, including the parametrium and regional lymph nodes. Fractionated delivery allows for cumulative tumoricidal doses while sparing normal tissues such as the bladder, rectum, and small bowel [17].

In recent years, the development of adaptive radiotherapy (ART) and specifically online adaptive EBRT has introduced a paradigm shift in how cervical cancer is treated. Traditional EBRT plans are based on baseline imaging and anatomical assumptions that may not hold true throughout the course of therapy. As tumors shrink and internal anatomy shifts due to organ motion or treatment response, static treatment plans can lead to underdosing of the tumor or excessive radiation to healthy tissues [18], [19].

Online adaptive radiotherapy addresses these limitations by incorporating daily imaging, such as cone-beam CT or magnetic resonance imaging (MRI), to adjust treatment plans in real-time. This adaptive approach enables clinicians to account for anatomical changes and ensure that radiation is delivered with maximal precision [18].

There are several advantages of online adaptive EBRT. First, there is dynamic target coverage, allowing continuous alignment between the evolving tumor and the radiation fields. Second, reduction of exposure to organs at risk (OARs), such as the rectum and bladder, through daily plan adaptation [17]. Third, mitigation of geometric uncertainties, including variations from bladder filling and bowel movement [17], [18]. Finally, the potential for safe dose escalation, enabling higher radiation doses to the tumor without increasing toxicity [18], [20].

Despite these advances, challenges remain in the widespread implementation of online ART. The need for daily imaging, increased planning complexity, and additional staff training are non-trivial barriers, particularly in low-resource settings [17], [21]. Nonetheless, the ability to personalize treatment with such precision represents a major clinical benefit and is increasingly becoming the standard of care in high-volume cancer centers [17], [22].

2.2.2 Chemotherapy

Chemotherapy serves as both a systemic and a radiosensitizing agent in the treatment of cervical cancer. When delivered concurrently with radiotherapy, it enhances the cytotoxic effects of radiation while also targeting potential micrometastatic disease [11], [23]. Cisplatin, administered on a weekly basis, is the most frequently used chemotherapeutic agent in this setting due to its favorable balance of efficacy and tolerability [24].

Multiple randomized clinical trials have demonstrated that the addition of cisplatin-based chemotherapy to radiotherapy significantly improves both progression-free survival and overall survival compared to radiotherapy alone. This benefit is particularly evident in patients with high-risk features such as lymph node involvement, parametrial extension, or bulky tumors [11], [25]. Chemotherapy is also employed in the adjuvant setting following surgery for patients with positive margins or high-risk pathological findings [24], [26].

However, this therapeutic enhancement comes at the cost of increased toxicity. Gastrointestinal distress, nephrotoxicity, and hematologic suppression are among the most common side effects. These side effects can pose challenges in patients with comorbidities or limited physiological reserve [24]. Additionally, the evidence base for chemotherapy is less robust in certain subgroups, such as patients with para-aortic nodal metastases, limiting its generalizability in those populations, [14]. In resource-limited environments, the logistical and economic demands of combined chemoradiotherapy may further constrain its application [22].

2.2.2 Brachytherapy

BT is a pivotal component of curative treatment in cervical cancer and is uniquely capable of delivering high doses of radiation directly to the tumor while sharply limiting exposure to surrounding healthy tissues [27], [28]. Unlike EBRT, which irradiates tissue from an external source, BT involves the placement of radioactive sources either within or immediately adjacent to the tumor. This proximity allows for an extremely high dose gradient, which is essential for eradicating tumor cells in the cervix and parametrial regions [27].

The introduction of image-guided adaptive BT (IGABT) has significantly enhanced the precision and effectiveness of this modality. By integrating advanced imaging, most commonly MRI but also CT, into each step of the treatment process, IGABT allows clinicians to visualize the tumor and surrounding anatomy with exceptional detail [28], [29]. This facilitates accurate delineation of the high-risk clinical target volume (HR-CTV) and OARs, enabling individualized dose planning and adaptive optimization throughout the treatment course [30].

Substantial to IGABT is that it adapts not only to the initial tumor configuration but also to dynamic changes in size and shape that occur in response to prior radiotherapy. This adaptability is particularly critical in cervical cancer, where substantial tumor regression during treatment is common [28], [31]. With IGABT, treatment plans can be modified to reflect these changes, ensuring consistent dose coverage of the tumor while avoiding excess radiation to the bladder, rectum, and bowel [29].

There are numerous clinical advantages of IGABT. The first is improved tumor control, ensuring the evolving tumor receives an adequate and conformal radiation dose throughout treatment [29], [32]. Second is personalized dose adaptation, accounting for anatomical variability between and within treatment sessions [16]. The third advantage is lower toxicity rates, due to more precise sparing of critical organs [27], [29]. The last advantage is enhanced suitability for complex cases, such as those involving extensive or irregular tumor spread [30].

Clinical evidence strongly supports the benefits of IGABT. Studies such as the Image guided intensity-modulated EBRT and MRI-based adaptive BT in locally advanced cervical cancer (EMBRACE) I trial have demonstrated significant improvements in local control, overall survival, and treatment-related morbidity compared to traditional 2D BT approaches [29], [33]. These data have led to the widespread adoption of IGABT as a best-practice standard in modern cervical cancer care [27], [30].

Nonetheless, the full potential of IGABT can only be realized when supported by robust clinical infrastructure, including access to MRI, standardized contouring protocols, applicator technology, and sophisticated treatment planning systems (TPSs). This underscores the need for ongoing research, training, and QA frameworks to ensure equitable implementation across diverse clinical settings [4], [34].

2.2.4 Clinical workflow of brachytherapy for cervical cancer

Initial evaluation and diagnostic work-up

All patients with locally advanced cervical cancer defined by FIGO as stage IB2 through IVA should be considered for BT as part of their definitive treatment [4], [35]. To ensure appropriate management, a comprehensive diagnostic evaluation must be conducted prior to treatment initiation.

Histopathologic confirmation via cervical biopsy is essential for diagnosis, as it determines tumor type (usually squamous cell carcinoma, adenocarcinoma, or adenosquamous carcinoma) and guides treatment planning. A clinical pelvic examination under anesthesia (EUA) is recommended by FIGO to establish clinical stage. This includes a bimanual pelvic exam to assess tumor size, vaginal involvement, and parametrial extension. EUA is also advantageous because it allows for a more thorough and pain-free assessment of the cervix and surrounding structures. Additionally, cystoscopy and sigmoidoscopy are performed when there is suspicion of bladder or rectal invasion, respectively. Identifying involvement of these organs is critical, as it may classify the disease as FIGO stage IVA and directly influences the therapeutic approach [36].

Bloodwork at baseline consists of three components. The first is a complete blood count to detect anemia, which is common in cervical cancer due to tumor-related bleeding. This can affect radiation tolerance [37]. Second is a basic metabolic panel, including renal function tests, since many patients may require cisplatin-based chemotherapy, which is nephrotoxic [4]. The last component is liver function tests to rule out hepatic dysfunction or metastatic disease, as well as to assess suitability for systemic therapy [4], [37].

In cases where there is hydronephrosis or ureteral obstruction, often caused by tumor extension to the pelvic sidewall or metastatic lymphadenopathy, intervention with ureteral stents or nephrostomy tubes may be necessary. These procedures restore urinary drainage and protect renal function before initiating chemoradiation [38], [5].

Together, all of these elements ensure a complete assessment of tumor extent, organ involvement, and patient suitability for radiation and concurrent chemotherapy, which are central to curative treatment [4].

Imaging and staging

While not explicitly required for FIGO staging, advanced imaging is indispensable in modern cervical cancer management, especially for treatment planning and prognosis.

MRI, particularly T2-weighted pelvic sequences, offers superior soft tissue contrast, enabling detailed delineation of the primary tumor, parametrial involvement, and local organ invasion. MRI has demonstrated staging accuracy ranging from 75% to 96% and it plays a central role in radiation therapy planning, both for EBRT and BT [39].

Positron Emission Tomography-Computed Tomography (PET/CT), performed with fluorodeoxyglucose (FDG), is the most sensitive imaging modality for identifying lymph node metastases and distant disease. It combines the metabolic imaging of PET with the anatomical localization of CT, making it superior to either modality alone for systemic staging. Studies have shown that nodal uptake on PET is highly prognostic, independently predicting progression-free survival [40], [41].

CT alone is often used for simulation and treatment planning but lacks the soft tissue resolution necessary for accurate local staging. Its role is primarily supportive unless MRI is contraindicated or unavailable [42].

PET/MRI is an emerging hybrid imaging modality that combines the metabolic insight of PET with the high-resolution soft tissue characterization of MRI. This integration offers the potential for improved detection of local tumor extent, parametrial involvement, and nodal metastasis in a single scan. PET/MRI may enhance treatment planning accuracy and reduce interobserver variability, particularly in centers with access to MRI-guided BT. Although not yet universally available and still under investigation for standard clinical protocols, PET/MRI is gaining traction in advanced cervical cancer staging workflows and may represent the future standard in comprehensive imaging [43].

Simulation and EBRT preparation

Once staging is complete and definitive radiotherapy is planned, patients undergo CT simulation for EBRT planning. Patients are positioned supine, typically with pelvic immobilization devices to enhance setup reproducibility. Intravenous contrast is often used to delineate pelvic vessels and oral contrast may be administered to visualize bowel loops. Patients are encouraged to present with a comfortably full bladder, which displaces the small bowel superiorly, thereby reducing radiation exposure to non-target tissues [44].

Before simulation, radiopaque markers or seeds are sometimes placed at the inferior extent of disease to aid in accurate field design. The decision between 3D conformal radiation therapy (3D-CRT) and intensity-modulated radiation therapy (IMRT) depends on institutional preference and patient-specific anatomy, though IMRT offers superior normal tissue sparing in many cases [45], [46].

Timing and integration of EBRT, chemotherapy, and BT

EBRT is delivered over approximately five weeks, typically in twenty-five to twenty-eight fractions (daily from Monday through Friday). Concurrent weekly cisplatin chemotherapy (40 mg/m^2) begins on Day one of EBRT. Importantly, cisplatin should be administered prior to EBRT on the same day and ideally at the start of the week. It should not be given on the same day as BT, nor should EBRT be scheduled on BT days [47].

BT may be started as early as week three of EBRT, but initiation is generally guided by tumor response and clinical judgment. Deferring BT until later in the course of EBRT allows for tumor shrinkage, facilitating improved applicator placement and reduced target volume. Regular pelvic examinations throughout EBRT are essential to monitor disease response and document residual tumor, often using clinical diagrams.

Concurrent chemotherapy mandates weekly blood monitoring, particularly to assess for neutropenia prior to BT procedures. BT should be delayed in the event of significant hematologic toxicity [47],[48].

A key principle in cervical cancer radiotherapy is that the overall treatment time (OTT), from the start of EBRT to completion of BT, should not exceed eight weeks. Prolonged OTT has been associated with roughly a 0.6–1% loss in pelvic control and overall survival per additional day, making timely coordination between modalities critical for optimal outcomes [46],[49].

2.2.4 Brachytherapy modalities

An essential consideration in the BT component of treatment for cervical cancer is the choice between HDR and low dose rate (LDR) techniques. Both modalities are effective in delivering tumoricidal doses to the cervix while sparing surrounding OARs, such as the bladder and rectum, but they differ significantly in logistical requirements, dose delivery, and patient experience.

Historically, LDR-BT was the standard of care. It involves continuous irradiation using radioactive sources such as Cesium-137 (^{137}Cs), delivered over one to three days, typically in one to two fractions. Dose rates are conventionally defined as less than 0.4 Gy/hour at point A. Due to the prolonged treatment time, patients must remain immobilized and hospitalized, often in radiation-protected rooms, which can be uncomfortable and resource-intensive. Despite these limitations, LDR has demonstrated excellent oncologic outcomes over decades of use [50], [51].

In recent years, HDR-BT has largely supplanted LDR in many centers, particularly in the United States and Europe. HDR utilizes Iridium-192 (Ir-192) as the radioactive source and employs remote afterloading technology, whereby a single high-activity source is driven robotically through multiple channels within the applicator. This allows for highly customizable dose distribution by modifying dwell positions and dwell times, a process often referred to as dose sculpting. The point A dose rate for HDR is more than 12 Gy/hour, with individual fractions typically lasting only a few minutes. Treatments are delivered on an outpatient basis, allowing for greater convenience, improved radiation safety for staff, and optimized patient throughput. According to a recent American Brachytherapy Society (ABS) survey, 85% of U.S. centers now utilize HDR-BT [52].

Despite differences in administration, clinical outcomes and toxicity profiles are comparable between HDR and LDR, when treatment is planned and delivered with the same level of precision [53]. HDR’s adaptability and logistical advantages have contributed significantly to its widespread adoption.

A third, less common modality is pulsed dose rate (PDR) BT, which serves as a hybrid between HDR and LDR. PDR uses a HDR source to deliver short pulses of radiation, typically once per hour during 2–3 days, mimicking the radiobiological effects of LDR while maintaining the logistical advantages of HDR (e.g., remote afterloading). Although it offers potential radiobiologic benefits, including better repair of sublethal damage in normal tissues, PDR still necessitates hospitalization and prolonged immobilization similar to LDR. It remains in use at select academic institutions in Europe and is not commonly employed in the United States [54], [55].

In practice, the choice between HDR, LDR, and PDR depends on institutional resources, clinician expertise, patient preference, and logistical considerations. However, given its flexibility, efficiency, and safety profile, HDR-BT has become the dominant modality in contemporary cervical cancer treatment. Table 1 gives an overview of the three different BT modalities.

Table 1: Overview BT modalities

Feature	HDR	LDR	PDR
Source	Ir-192	Cs-137	Ir-192
Dose rate (point A)	>12 Gy/hour	<0.4 Gy/hour	0.5–1.0 Gy/hour (in pulses)
Delivery method	Remote afterloading	Manual or remote afterloading	Remote afterloading (pulsed hourly)
Fraction duration	Minutes	Continuous (24–72 hours)	Pulses hourly over 2–3 days
Number of fractions	3–5	1–2	1–2
Hospitalization required	No	Yes	Yes
Patient immobilization	Brief, per fraction	Prolonged (1–3 days)	Prolonged (similar to LDR)
Radiation safety	Minimal exposure to staff	Radiation exposure to staff possible	Minimal exposure to staff
Flexibility / dose sculpting	High (custom dwell times and positions)	Limited	Moderate (some modulation possible)
Availability / use	Widely used (dominant in most centers)	Declining use	Rare, mainly in select European centers
Radiobiologic effect	Less continuous (high dose per fraction)	Continuous low dose	Mimics LDR biologically
Clinical outcomes	Comparable to LDR	Long-standing efficacy	Comparable where used

2.2.5 Treatment planning systems in brachytherapy

The TPS forms the computational backbone of BT, linking anatomical geometry to dosimetric delivery. They are responsible for defining the spatial distribution of radiation dose based on applicator configuration, source characteristics, and patient-specific imaging data. In both EBRT and BT, the TPS is where clinical intent is translated into quantitative treatment parameters. However, in brachytherapy, where dose gradients are extremely steep and anatomy is tightly coupled to source positioning, the accuracy and resolution of TPS calculations are particularly critical [56].

In modern gynecological BT, TPS workflows typically begin with volumetric imaging, such as CT or MRI, which is used to reconstruct the patient anatomy and applicator geometry. These images are then segmented to define structures like the HR-CTV, OARs, and the applicator channels. The TPS uses this geometric data to simulate dose distributions using algorithms based on either the standard Task Group 43 (TG-43) formalism of AAPM or more advanced model-based dose calculation algorithms (MBDCAs) such as Acuros BV or Monte Carlo simulations [57].

A core challenge in this process is ensuring that the geometric representation of the applicator, including its position, curvature, and source channel path, is accurate. Any deviation in geometry can directly impact dose calculation, particularly in high-gradient regions. This is why phantom-based QA, as explored in this thesis, is essential. By replicating the treatment geometry in a controlled phantom and comparing calculated doses to measured values, the performance and limitations of the TPS can be independently validated [58].

Moreover, the integration of CT-derived geometry with physical phantom measurements enables spatially resolved QA. For example, deviations in applicator channel printing or deformation in flexible materials (e.g., TPU) can be evaluated against CT reconstructions. These geometric features are then fed into the TPS to assess how dimensional variations translate into dosimetric uncertainty. This way, the TPS acts as a bridge between imaging and dose and is therefore central to both treatment accuracy and QA [59].

In this project, both TG-43 and model-based algorithms were used to compute expected dose distributions in PLA and TPU phantoms. The outputs were compared to real-world measurements using plastic scintillators and film dosimetry. This enabled a side-by-side evaluation of the TPS assumptions and confirmed the value of geometry-aware QA using 3D-printed models [60].

2.3 Role of 3D printing in brachytherapy

3D printing, also known as additive manufacturing, has gained significant traction in the medical field due to its ability to produce patient-specific models, implants, and training tools with a high degree of customization and precision. Its applications span from surgical planning to prosthetics and radiation therapy, where anatomical complexity and individualization are critical. In radiotherapy specifically, 3D printing enables the fabrication of custom accessories and phantoms for QA and treatment optimization, offering cost-effective solutions for personalized care [10].

Several 3D printing technologies are available, each with distinct advantages and limitations in terms of resolution, mechanical properties, material compatibility, and cost. The most commonly used methods in medical applications will be discussed.

FDM

FDM is among the most accessible and widely used 3D printing technologies. It works by extruding thermoplastic filaments through a heated nozzle, depositing material layer by layer to form the final object. Materials such as PLA and TPU are commonly used. PLA is known for its ease of use, dimensional stability, and low cost, making it well-suited for rigid structures. In contrast, TPU and other flexible filaments are used when elasticity is required to simulate soft tissue properties. While FDM generally offers lower resolution than other techniques, it remains ideal for rapid prototyping and functional medical models [10], [61].

Stereolithography (SLA)

SLA uses a laser to cure liquid photopolymer resin into solid objects with high resolution and surface smoothness. It is particularly suited for detailed anatomical models where fine structural fidelity is necessary. However, SLA-printed parts may require additional post-processing (e.g., cleaning and UV curing), and the resins used are often more brittle than thermoplastics [62].

Selective laser sintering (SLS)

SLS employs a laser to sinter powdered materials, such as nylon or other polymers, into solid objects. This technique does not require support structures and offers good mechanical strength and geometric flexibility. However, the process is more costly and less accessible for routine phantom production in most clinical environments [63].

In this project, FDM printing was selected as the preferred method due to its widespread availability, simplicity, and compatibility with both rigid and flexible materials. The phantom was printed twice: once using PLA to represent a stable, non-deformable model, and once using TPU to simulate soft-tissue deformation. This dual-material approach allows for comparative evaluation of mechanical properties and dosimetric performance, supporting the development of a reproducible and practical tool for BT QA [10], [64].

2.3.2 3D-printed applicators in brachytherapy

The integration of 3D printing into BT has revolutionized the design and fabrication of applicators, especially in the treatment of cervical cancer. Traditional, commercially available applicators often lack the adaptability required to accommodate the diverse anatomical variations and tumor topographies encountered in patients. This limitation can compromise dose distribution and patient comfort. In contrast, 3D-printed applicators offer a customizable solution, tailored to individual patient anatomy, thereby enhancing treatment efficacy and safety [65].

In cervical cancer BT, the use of 3D-printed applicators has become increasingly prevalent. These applicators are designed based on imaging data, allowing for precise conformity to the patient's anatomy. This precision facilitates optimal placement of radiation sources, ensuring effective dose delivery to the tumor while minimizing exposure to adjacent healthy tissues. Studies have demonstrated that 3D-printed applicators can significantly improve dosimetric parameters, such as D90 and V100, without exceeding dose constraints for OARs [66], [67].

Furthermore, the application of 3D-printed templates in interstitial BT (ISBT) has shown promise. These templates guide needle placement with high precision, reducing the risk of complications associated with freehand needle insertion. The use of 3D-printed templates has been related to improved dose conformity and reduced radiation exposure to critical structures [58].

The workflow for creating 3D-printed applicators involves several steps: image acquisition (typically MRI or CT), treatment planning, applicator design using computer-aided design (CAD) software, and fabrication using biocompatible materials suitable for sterilization. Materials commonly used include PLA and photopolymer resins, chosen for their mechanical properties and compatibility with sterilization processes [10].

In conclusion, the adoption of 3D-printed applicators in cervical cancer BT represents a significant advancement in personalized medicine. By accommodating individual anatomical variations and enabling precise dose delivery, these applicators enhance treatment outcomes and patient safety. As 3D printing technology continues to evolve, its role in BT is expected to expand, offering new possibilities for customized cancer treatment.

2.3.3 3D-printed phantoms for QA in cervical cancer brachytherapy

QA plays a central role in ensuring safe, effective, and reproducible treatment delivery in BT. In cervical cancer, where applicator placement, dose gradients, and organ proximity are highly variable, the need for robust QA tools is particularly acute. Conventional phantoms, while useful for generalized QA, are often limited by their lack of adaptability, cost, and inability to replicate realistic treatment geometries. In this context, 3D printing has emerged as a promising technology for developing custom, application-specific QA phantoms.

A small number of studies have explored the use of 3D-printed phantoms, specifically for QA in cervical BT, and those that do exist primarily focus on imaging validation or dosimetric comparisons. One notable example is a study by Kirisits *et al.*, in which a multi-purpose QA phantom was designed for MRI-based gynecological BT. This phantom achieved dose discrepancies of less than 1.7% compared to TPS calculations and demonstrated volumetric accuracy for OARs within 1.1% on average. Geometric deviations remained under 0.7 mm compared to CT-based reconstructions, highlighting its reliability for QA purposes [58].

However, despite these promising results, the overall number of published studies in this specific area remains low. Most existing literature related to 3D printing in BT centers around custom applicators, with far fewer efforts dedicated to phantom development for QA. This represents a clear gap in the field, one where systematic, reproducible, and low-cost QA tools are urgently needed, especially as IGABT becomes more prevalent [65].

The current study contributes directly to addressing this gap by developing a non-anatomical, reproducible 3D-printed phantom designed specifically for QA audits in cervical cancer BT. Unlike most previous studies, this phantom is evaluated not only for structural or imaging performance but also through direct dosimetric testing using two different materials (rigid PLA and flexible TPU). By comparing how material properties influence dose distribution and imaging performance, this work provides valuable data for future implementations and standardizations of QA phantoms in clinical and training settings.

From a QA perspective, 3D-printed phantoms offer several distinct advantages, four will be discussed. The first advantage is custom geometry, meaning the phantoms can be designed to match specific test configurations, including applicator geometries and imaging constraints. Second is material flexibility that offers broader test scenarios since different print materials can simulate varying tissue densities and deformation behavior. The third advantage is the low cost and reproducibility. Once designed, phantoms can be printed repeatedly with minimal cost and low inter-institutional variability, supporting widespread QA audits [66]. The last advantage is imaging compatibility. Depending on the material used, phantoms can be compatible with both CT and MRI workflows, making them suitable for multi-modality QA [67].

By directly addressing the underexplored area of QA-specific phantoms for cervical BT, this project highlights the broader potential of 3D printing to improve not only clinical customization but also treatment reliability, staff training, and long-term audit processes. The work presented here is intended as a step toward establishing practical, evidence-based guidelines for phantom development that can be applied and reproduced across institutions.

2.4 Dosimetric testing

2.4.1 Purpose of dosimetric audits

In modern BT, the delivery of radiation dose is highly localized and occurs within steep spatial gradients. As a result, even small uncertainties in source positioning, treatment planning, or dose calculation can lead to clinically significant deviations. Dosimetric audits are essential tools in QA protocols, enabling verification that the prescribed dose is delivered accurately and consistently. They play a critical role in validating the end-to-end workflow from imaging and planning to actual dose delivery [68].

The need for audits is heightened in HDR-BT, where treatment fractions are short and highly concentrated. Detecting errors in such settings may not be evident without physical measurement. Dosimetric audits serve to independently confirm that systems are calibrated correctly, dose calculation models are reliable, and that the delivered treatment matches what was planned. Regulatory guidelines and professional societies such as the AAPM recommend regular dosimetric auditing as part of routine clinical QA programs, especially when introducing new techniques, sources, or dose calculation algorithms [6].

Moreover, dosimetric audits help identify inter-institutional variability in treatment delivery, serving as a benchmark for consistency and safety. These audits not only uncover errors but also drive improvements in clinical workflows, detector calibration, and dose modeling accuracy. As new MBDCAs and imaging-guided workflows become integrated into practice, the role of dosimetric auditing is expanding in both clinical and research settings [69].

2.4.2 Role of phantoms in QA

Phantoms serve as indispensable tools in dosimetric testing and QA. These physical models are designed to simulate human tissue in both geometry and radiological properties, providing a controlled environment for evaluating dose delivery systems. In BT, phantoms are particularly useful for replicating anatomical setups, testing applicator placement, and verifying the accuracy of dose distributions calculated by TPSs [70].

Various types of phantoms exist for different QA purposes. Water phantoms are often used for fundamental source characterization due to their close equivalence to the medium assumed in TG-43 calculations. Solid phantoms are commonly constructed from materials such as Poly(methyl methacrylate) Acrylonitrile butadiene styrene, PLA, or TPU. These materials are chosen for their reproducibility, ease of machining, and compatibility with integrated dosimetry systems. These phantoms can be customized with cavities or channels to accommodate applicators, dosimeters, and film inserts, enabling precise dose measurements at clinically relevant positions [71].

Phantoms also facilitate the evaluation of complex dose distributions, especially in high-gradient regions near BT sources. When used with detectors like film or plastic scintillators, phantoms provide spatially resolved or real-time dose data that can be directly compared to planned values. This makes them essential for commissioning model-based dose calculation algorithms, conducting end-to-end workflow tests, and performing routine QA assessments [72].

The phantom developed in this project was specifically designed for BT QA, incorporating dual channels to accommodate both a plastic scintillator and a BT applicator. Its compact size and modular construction allow for fixed, reproducible placement of detectors, one for the plastic scintillator and one for film, supporting repeated measurements under controlled conditions. By mimicking clinical setups in a reproducible format, this phantom supports objective validation of dose calculation models and delivery accuracy in gynecological HDR-BT.

2.4.3 Plastic scintillator dosimetry: real-time dose verification

Plastic scintillator detectors (PSDs) are highly effective tools for point-based, real-time dosimetric verification in BT [72]. These detectors consist of a small scintillating element connected to a light-transmitting fiber, which carries the scintillation light produced by ionizing radiation to an external photodetector. The light intensity is proportional to the absorbed dose, allowing for continuous monitoring of radiation delivery.

The primary advantages of PSDs in BT include their near water-equivalence, small active volume, and real-time dose readout [73]. These characteristics make them especially useful for HDR treatments, where rapid feedback can identify discrepancies in dwell time, source positioning, or unexpected interruptions during irradiation.

In this project, a plastic scintillator was positioned in a dedicated channel of the PLA phantom to measure dose at a defined reference location. Prior to use, the system was calibrated using a known radiation source under similar energy conditions to those expected during treatment. Calibration ensures the signal-to-dose relationship is accurate, accounting for any light losses or spectral effects within the optical fiber system.

One notable challenge in PSD systems is the presence of Cherenkov radiation, or the 'stem effect', which occurs when the optical fiber itself emits light during irradiation. To address this, modern systems use spectral separation techniques or dual-channel correction algorithms to isolate and subtract the Cherenkov contribution from the total signal, leaving only the true scintillation component [72].

The plastic scintillator setup in this project provided time-resolved dose information that can be directly compared to the expected dose profile from treatment planning. This allows for not only absolute dose verification but also dynamic validation of source dwell times and positional accuracy, all critical aspects of HDR-BT QA [74].

2.4.4 Dose calculation models: TG-43 vs. model-based algorithms

Accurate dose calculation is fundamental to the success of BT treatments. Historically, the most widely used approach has been TG-43 formalism. TG-43 provides a standardized method for calculating the dose around BT sources, based on pre-measured or Monte Carlo-derived parameters in a uniform water phantom [75]. It assumes an isotropic source in an infinite water medium, neglecting patient-specific factors such as tissue heterogeneity, applicator attenuation, or anatomical boundaries.

While TG-43 has been clinically useful and broadly validated, its simplifying assumptions can lead to significant discrepancies in certain treatment scenarios. These include treatments involving complex applicator materials, proximity to air or bone interfaces, and large or irregular treatment fields. In such cases, TG-43 may overestimate or underestimate the actual dose, especially in regions of sharp density gradients [76].

To address these limitations, MBDCAs such as Monte Carlo simulations and deterministic solvers like Acuros BV have been introduced [77]. These algorithms solve the linear Boltzmann transport equation or simulate particle transport to account for heterogeneities in patient anatomy and materials. As recommended by AAPM’s TG-186, MBDCAs enable more realistic dose calculations by incorporating CT-based tissue densities, applicator geometries, and shielding effects [77].

In this context, dosimetric validation using phantoms becomes essential. Since MBDCAs calculate dose distributions in complex, patient-like geometries, measurements in controlled phantom environments help verify their accuracy. Film dosimetry and plastic scintillators are particularly useful in benchmarking the calculated dose from TG-43 and MBDCAs against actual measured dose, helping clinicians understand the expected differences and identify situations where MBDCA implementation offers a clear clinical advantage.

In this project, only TG-43 was used to simulate the expected dose distribution within the phantom. Comparisons between these calculations and experimental measurements with the plastic scintillator and film are used to assess the limitations of TG-43.

2.4.5 Film dosimetry

Radiochromic film dosimetry is widely used in BT due to its high spatial resolution, near tissue-equivalence, and ease of use. These self-developing films darken in response to ionizing radiation and can be scanned and analyzed to provide two-dimensional dose distributions. Among them, Gafchromic™ EBT3 (Ashland™) is a popular choice, offering minimal energy dependence and water equivalence suitable for HDR applications [78].

Film dosimetry plays an important role in QA and end-to-end testing. Unlike point detectors, film captures the full dose profile in a given plane, which is especially beneficial in treatments with steep dose gradients and complex geometries, such as HDR gynecological BT. Films are typically placed in phantoms and irradiated under known conditions. Post-irradiation, the optical density is scanned and converted to dose using a calibration curve from known exposures [78].

In this project, film dosimetry was employed for the TPU phantom. While the phantom included a dedicated channel for a plastic scintillator, its flexible material properties introduced challenges for dosimetric accuracy. The scintillator was calibrated using TG-43 formalism, which assumes water-equivalent material. However, CT imaging of the TPU phantom revealed that it was neither fully water-equivalent nor homogeneous in density. These findings raised concerns about the validity of scintillator measurements alone [72]. Therefore, film dosimetry was introduced as a complementary method to validate the delivered dose, offering an independent, planar measurement not reliant on water-equivalence assumptions or real-time calibration constraints [78], [79].

The film was inserted between the two horizontally separated halves of the phantom, which were designed to hold it securely and align it with the applicator and source channel.

The film-based measurements allowed a planar verification of the delivered dose against the calculated dose distributions from both TG-43 and model-based algorithms. While lacking the real-time capability of scintillator systems, film dosimetry provided comprehensive spatial information, which is especially valuable for detecting angular discrepancies, shielding effects, or unexpected source displacements [78].

The integration of film into the TPU phantom proved beneficial for validating the planned dose distribution under flexible phantom conditions. Despite some surface imperfections from the printing process, the film interface remained adequately aligned, ensuring that deviations in dose delivery could be confidently attributed to physical or algorithmic sources rather than measurement error.

2.4.6 Uncertainties and deviations quantified by phantom tests

Dosimetric testing using phantoms allows not only for confirmation of expected dose distributions, but also for the identification and quantification of key uncertainties and deviations within the treatment workflow. These can originate from geometric errors, calibration limitations, material inhomogeneities, or algorithmic simplifications. By integrating detectors such as plastic scintillators and film into a phantom environment, multiple dimensions of potential inaccuracy can be assessed [27], [72].

One common source of uncertainty is applicator misplacement or angulation, which can lead to substantial dose discrepancies in high-gradient regions typical of HDR brachytherapy. Phantoms with fixed channels, like the one used in this study, are effective in testing the reproducibility of applicator positioning and its impact on dose delivery. Even small angular deviations can alter source-to-detector distances, influencing both absolute dose and spatial gradients [7].

Material properties of the phantom itself also contribute to measurement variability. As seen with the TPU phantom, deviations from water equivalence and density inhomogeneities affected dose absorption and detector response [72]. These variations complicate direct comparison with TG-43-based calculations, highlighting the importance of using measurement tools such as film for independent validation [78].

Another key source of deviation arises from the differences between TG-43 and model-based algorithm calculations. Phantom measurements allow for side-by-side comparisons between calculated and measured doses, offering insights into where TG-43 may over- or underestimate dose, especially near applicator boundaries, in the presence of air cavities, or at interfaces between different materials [75], [77].

Scintillator and film data also reveal dose uncertainties associated with real-time delivery, such as irregular source dwell times or incomplete delivery due to interruptions. These are difficult to capture in planning software but are made visible through continuous measurement and post-irradiation imaging [74], [78].

Together, these measurements help define the expected margins of error for brachytherapy delivery systems and offer guidance on when corrective measures or more sophisticated planning models are warranted. In this project, the phantom enabled such analysis, forming the basis for future refinement of phantom-based auditing protocols in gynecological HDR-BT.

3. Methods

3.1 Phantom model development

This section describes the development of two 3D-printed QA phantoms designed for gynecological BT: one printed in rigid PLA (REAL filament black, 1.75 mm) , and one in flexible TPU (70A Filaflex Navy Blue Ultra-Soft, 1.75 mm). While both phantoms share the same anatomical and geometric basis, differences in material behavior and printer settings necessitated design adaptations and distinct workflows. The development process is organized into six stages: design, stereolithography (STL) conversion, slicing, print preparation, printing, and post-processing.

3.1.1 Design creation

The initial stage in the additive manufacturing process involves transforming conceptual or clinical requirements into a functional 3D model using CAD software. This phase is both technical and creative, requiring careful attention to geometry, tolerances, and manufacturability. Material properties and printer capabilities strongly influence this step, as the design must anticipate how the chosen polymer will behave during printing and under use conditions.

The complexity of a design is often dictated by the mechanical characteristics of the material. For instance, rigid polymers like PLA can support sharper geometries and tighter tolerances, whereas flexible materials like TPU may benefit from smoother transitions to reduce stress concentrations, while allowing for tighter channel fits due to their capacity to deform elastically. Moreover, the selected 3D printing method, FDM in this case, imposes its own constraints. Layer height, resolution, and build volume, as well as the tendency for certain materials to warp or string, all factor into how the model must be structured. These limitations must be considered early, including the need to avoid overhangs that would require supports and the importance of orientation of different parts to minimize print artifacts.

In this context, the PLA phantom was designed first and served as the reference model. The process began with a CT scan of a commercially available BT applicator, using a slice thickness of 1 mm. This scan was segmented in 3D Slicer to isolate the applicator from surrounding material. Due to mesh complexity and software limitations, the applicator was manually reconstructed in Fusion 360 (Figure 1).

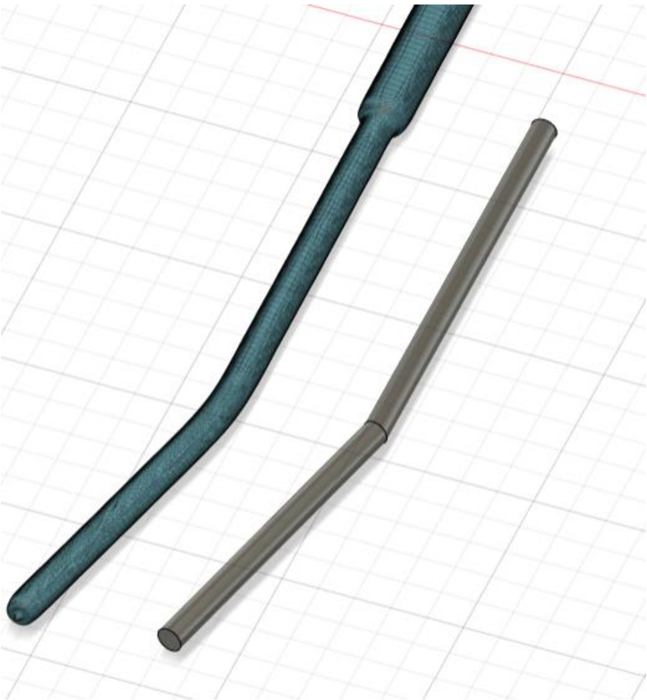

Figure 1: STL and rebuilt CAD model of applicator

The CAD model of the phantom itself, including all internal and external geometry, was also created in Fusion 360 to maintain design consistency and control over all dimensional parameters. Based on this CAD model, a full phantom was designed with dual channels, one for the applicator and one for a plastic scintillator. The phantom was split into two horizontal parts, with the bottom part containing the U-shaped channels (Figure 2). This design choice simplified insertion and accommodated for film dosimetry.

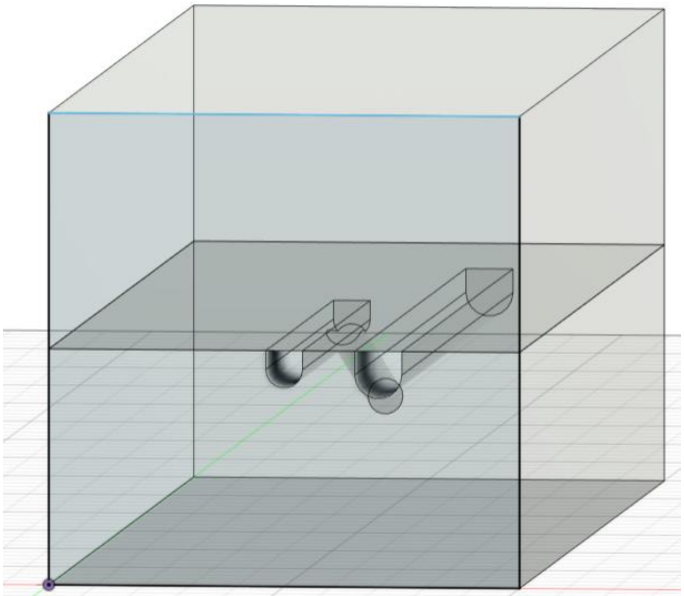

Figure 2: CAD model with two distinct parts and U-shaped channels

Additionally, the overall size of the phantom was deliberately reduced to 5 cm × 5 cm × 15 cm to minimize print time and material usage. While this reduction improved production efficiency, it came at the expense of phantom volume, which may limit the accuracy of backscatter conditions during dosimetric evaluation. This trade-off was considered acceptable for the purpose of early-phase validation. To optimize fit, a margin test block (Figure 3) was printed to identify the appropriate clearance between the applicator and the printed channel. A channel diameter of 3.9 mm was selected as the best compromise between ease of insertion and minimal air gaps.

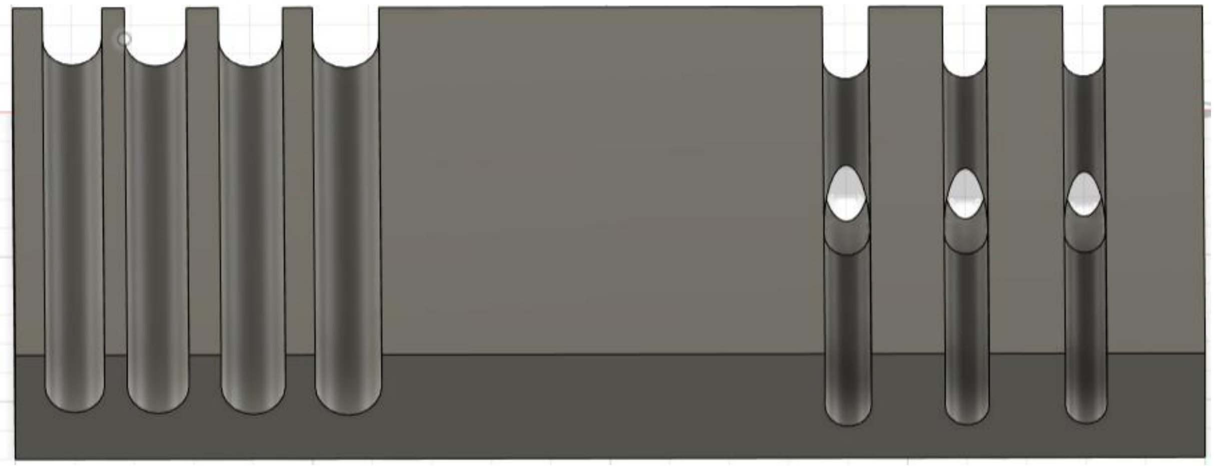

Figure 3: Margin test block

The TPU phantom was developed through a slightly different workflow. Instead of starting from scratch, the PLA phantom served as the baseline model. A CT scan of the printed PLA phantom was used to verify internal and external dimensions. From this data, the channel geometry was slightly modified: while PLA required increased clearance to account for surface roughness and rigid tolerance, TPU's flexible nature allowed the applicator to be inserted even with a tighter fit. This material behavior permitted a slight reduction in channel diameter compared to the PLA version, improving surface contact and reducing air gaps while still allowing smooth insertion due to elastic deformation. A diameter of 3.7 mm was chosen for this reason. No major structural changes were required for the TPU version, but the modified channel dimensions reflected material-specific behavior during insertion and use.

Each design was constrained by the build volume of the printer it was intended for, with the PLA phantom printed on the Creality K1 Max and the TPU phantom on the Creality Ender 3 S1, which has a smaller build area and optimized for printability without supports. Internal radii were smoothed, sharp corners were avoided, and channel paths were curved to follow the applicator's geometry. These shared design principles, combined with material-specific adjustments, ensured that both phantoms remained functionally equivalent while accounting for distinct mechanical properties.

3.1.2 Conversion to STL

Once the CAD designs for both phantoms were finalized in Fusion 360, they were exported as STL files , a standard format widely used in additive manufacturing. STL files represent the external surface geometry of a 3D object using a mesh of triangles, a process known as tessellation. This method approximates curved surfaces into a faceted structure, which allows the model to be interpreted by slicing software for layer-by-layer fabrication.

Unlike native CAD files, which define geometry through mathematically precise solids and parametric features, STL files translate these forms into a simplified mesh structure. Slicing software cannot directly process complex CAD data because it lacks the computational methods to interpret volumetric solids or constraints. Instead it requires a mesh-based representation to generate toolpaths for the printer. This makes STL a critical intermediary format in the additive manufacturing workflow.

In this project, STL export settings were chosen to maintain the resolution of the model while avoiding excessive mesh density that could slow down processing or introduce slicing errors. The fine detail of the internal channels for both the applicator and scintillator was preserved, and no smoothing or simplification was applied. This ensured dimensional accuracy and geometric fidelity, which are essential for quality assurance applications.

Although STL files do not retain material information, color, or metadata, this limitation was not relevant for this use case. All material-specific adjustments, such as the wider channel for PLA or the tighter fit for TPU, were incorporated at the CAD stage, so the exported geometry was already optimized.

This step ensured that both phantoms could be reliably sliced and printed with minimal risk of data loss or deformation, preserving the functional intent of the original design.

3.1.3 Slicing

Once the STL files were generated, they were imported into slicing software to convert the 3D models into machine-readable instructions. For the PLA phantom, OrcaSlicer was used because of its user-friendly interface, making it especially suitable for initial slicing tasks and straightforward prints like those involving rigid PLA. In contrast, the TPU phantom was sliced using IdeaMaker, which offered more precise control over print settings specific to flexible filaments and allowed for deeper customization once more experience was gained. This process, known as slicing, divides the model into successive horizontal layers and generates G-code, which defines the printer's movement, extrusion rate, and temperature control for each layer. Slicing plays a crucial role in ensuring that the printed object faithfully reproduces the intended geometry and mechanical behavior, especially for phantoms where internal accuracy is critical.

Each material required a tailored slicing profile due to differences in flow behavior, thermal expansion, and printability. For PLA, the objective was to maintain dimensional accuracy and surface quality. The slicing profile included a rectilinear infill pattern at 90% density, a layer height of 0.2 mm, and a line width of 0.42 mm. The extruder temperature was set to 220 °C and the flow rate was adjusted to 93% to avoid over-extrusion. The print speed was set to 30 mm/s, providing a balance between quality and build time. Support structures were disabled, as the model was designed to avoid overhangs (Table 2).

Table 2 Slicing settings PLA phantom

Parameter	**Value**
Infill Pattern	Rectilinear
Infill Density	90%
Layer Height	0.2 mm
Line Width	0.42 mm
Extruder Temperature	220 °C
Flow Rate	93%
Print Speed	30 mm/s
Support Structures	Disabled

TPU, being flexible and prone to deformation during printing, required a significantly more conservative slicing strategy. IdeaMaker was selected as the slicing software instead of OrcaSlicer, as it provided more granular control over parameters relevant to flexible filament behavior. While slicing settings for PLA were based on values reported in the literature for high-density, water-equivalent phantoms, much less information was available for TPU in general, and the available data often lacked specificity regarding filament brand and type. This is particularly relevant as TPU properties can vary significantly depending on color and formulation. For instance, the slicing settings used here were based on Filaflex 70A Navy, a filament whose radiological and mechanical properties differ from other colors within the same product line. As a result, generalized recommendations were insufficient, and print parameters had to be experimentally determined for this specific filament. Therefore, slicing settings for TPU were determined through a series of experimental test prints starting from prior investigations already done at Maastro (Table 3).

Table 3: TPU material analysis results

Filaflex filament	**Infill density [%]**	**Z_{eff}**	**Std dev.**	**80 kV**	**Std dev.**	**140 kV**	**Std. dev.**	**RED**	**Std. dev.**
70 A Navy	100	7.98	0.26	104	9	83	9	1.07	0.01
	60			-233	33	-237	34	0.75	0.04
	30			-607	16	-615	16	0.38	0.02
	20			-747	14	-751	15	0.25	0.02
	10			-873	59	-876	65	0.12	0.07
70 A Black	100	6.58	0.39	-13	58	4	59	1.02	0.06
	60			-382	27	-370	28	0.64	0.03
	30			-689	13	-683	15	0.32	0.02
	20			-787	13	-782	16	0.22	0.02
	10			-894	53	-893	60	0.11	0.07
60 A Pro Black	100	6.13	0.40	-25	22	2	22	1.03	0.02
	60			-411	45	-396	48	0.62	0.05
	30			-716	29	-709	31	0.30	0.03
	20			-805	22	-799	26	0.21	0.03
	10			-909	52	-907	57	0.09	0.06

Based on the observed trends, an infill range between 86% and 94% with a gyroid pattern was initially selected to approach Hounsfield units (HU) of 0 and relative electron density (RED) of 1 (Figure 4 and Figure 5). However, CT analysis of these test cubes revealed lower HU values than predicted and showed internal inhomogeneity (Figure 6 and Table 4). To improve homogeneity, the infill pattern was changed to a line structure and new cubes were printed at similar densities. The line pattern produced comparable results but offered more consistent internal structure (Table 5). Ultimately, a line infill at 98% density was selected for the TPU phantom to balance mechanical flexibility and water equivalence.

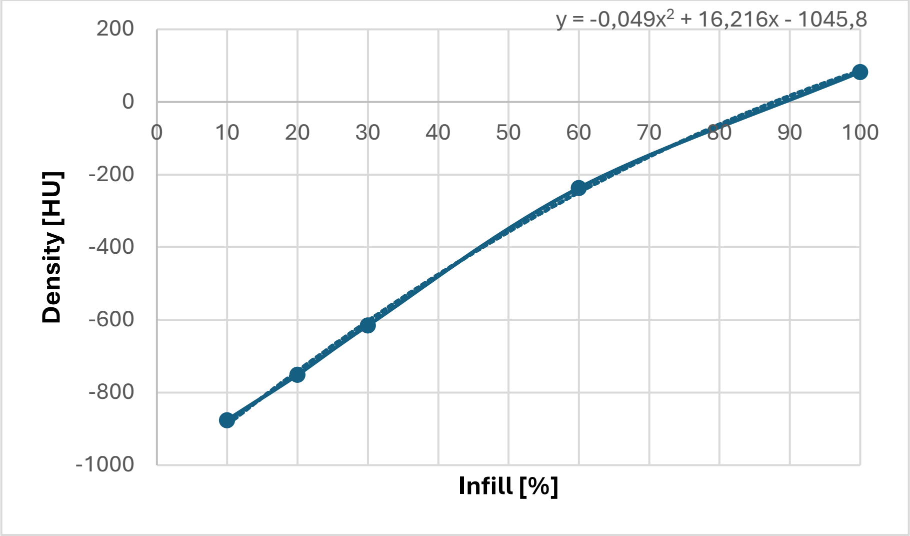

Figure 4: Relation infill to density test cubes

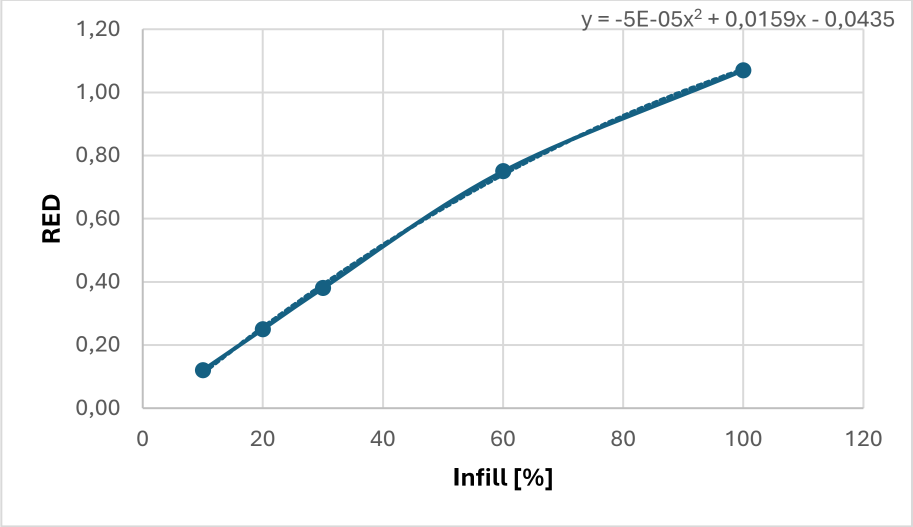

Figure 5: Relation infill to RED test cubes

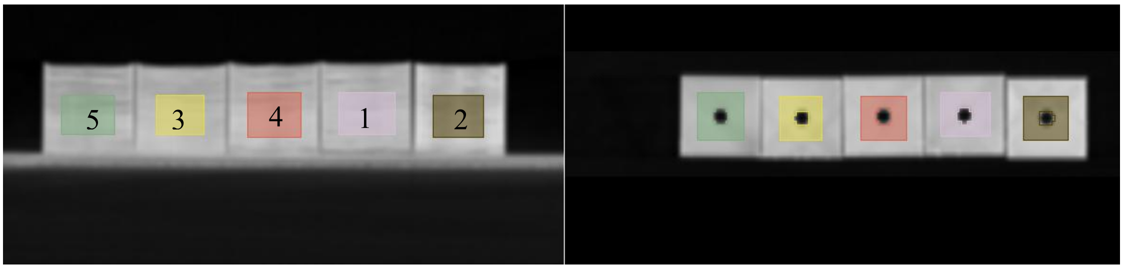

Figure 6: Test cubes ranging from 86 to 94% infill

Table 4: Gyroid test cube analysis

No.	Segment	Minimum [HU]	Maximum [HU]	Mean [HU]	Std dev. [HU]
1	Cube 86 infill	-358	79	-73.0433	85.4111
2	Cube 88 infill	-361	64	-116.44	82.4583
3	Cube 90 infill	-357	2	-108.781	54.3176
4	Cube 92 infill	-361	35	-75.5158	63.64
5	Cube 94 infill	-261	73	-50.7104	40.9787

Table 5: Line test cube analysis

No.	Segment	Minimum [HU]	Maximum [HU]	Mean [HU]	Std dev. [HU]
1	Cube 86 infill	-454	-6	-159.96	64.1785
2	Cube 88 infill	-458	-23	-136.861	69.1633
3	Cube 90 infill	-376	-8	-102.749	59.5668
4	Cube 92 infill	-414	5	-107.763	50.5423
5	Cube 94 infill	-458	78	-63.7346	77.1453

The final slicing settings included a layer height of 0.18 mm and an extrusion width of 0.22 mm. Print speeds were set to 22.5 mm/s for all regions. Retraction was enabled with a retraction distance of 2 mm, speed of 20 mm/s, and a Z-hop of 0.4 mm. A brim was used to assist bed adhesion. The extruder temperature was set to 240 °C. Flow rate was increased to 145% for infill to enhance internal solidity and improve attenuation properties. These settings were optimized to produce stable prints while approaching the radiological behavior of water (Table 6).

Table 6: Slicing settings TPU phantom

Parameter	Value
Layer Height	0.18 mm
Extrusion width	0.22 mm
Print Speed	22.5 mm/s
Retraction	Enabled
Retraction Distance	2 mm
Retraction Speed	20 mm/s
Z-Hop	0.4 mm
Extruder Temperature	240 °C
Infill Flow Rate	145%

By adapting the slicing parameters to suit each material, this stage helped bridge the gap between virtual geometry and physical implementation, enabling both phantoms to be manufactured with accuracy and repeatability.

3.1.4 Print preparation

The steps required to prepare the printer and materials before fabrication varied significantly depending on the material used. PLA, being a rigid and widely used filament, required only minimal preparation. The print bed of the Creality K1 Max was cleaned using isopropyl alcohol to ensure proper adhesion of the first layer. The filament was loaded directly without any drying process, as PLA is not particularly hygroscopic. Manual bed leveling was performed prior to printing to ensure uniform nozzle distance. The slicer-generated G-code was then transferred to the printer and the first layer was visually monitored to confirm proper adhesion and extrusion behavior.

In contrast, preparing the print for TPU required a more controlled and cautious workflow due to the material's sensitivity to environmental conditions and extrusion dynamics. TPU filament, specifically Filaflex 70A Navy, is hygroscopic and must be dried thoroughly before printing. For this project, the filament was dried at 60 °C for several hours to reduce the risk of bubbling, stringing, and inconsistent extrusion. The Creality Ender 3 S1 printer was then prepared with adjusted extruder tension to ensure proper grip on the flexible filament without deformation. Additionally, to prevent the phantom from curling or detaching during printing, the base of the TPU print was manually glued to the print bed using a removable adhesive, ensuring stable adhesion throughout the process.

Prior to printing the full phantom, a series of calibration prints were performed. This began with basic extrusion test cubes to verify dimensional accuracy and check for under- or over-extrusion. After initial validation, short channel segments from the phantom model were printed to evaluate channel fidelity and ensure that the applicator would fit without resistance or structural compromise. These preparatory steps helped ensure that the customized TPU slicing profile would perform reliably over the full-length phantom print.

3.1.5 Printing the phantom

The PLA phantom was printed on a Creality K1 Max equipped with a 0.4 mm nozzle. The full phantom, divided into two horizontally split parts, was printed successfully on the first attempt. The print exhibited consistent quality across both halves, with no visible warping, delamination, or surface defects. Internal channels for both the applicator and scintillator were well-resolved and dimensionally accurate. The total print time was approximately 10 hours. After printing, the parts were easily removed from the bed without requiring any post-processing or adjustments.

The TPU phantom, by contrast, was printed on two Creality Ender 3 S1 printers in parallel to reduce print time. The top and bottom halves were printed simultaneously on separate machines, effectively reducing the total print time from approximately 125 hours to about 62.5 hours. While this approach improved efficiency, it introduced further challenges.

Clogs occurred repeatedly during test prints and also during the first attempt to print the full phantom, leading to a failed print. These issues were attributed to the flexible nature of TPU and required a second full print. The second attempt was successful, though overall print quality remained inferior to the PLA phantom. Differences in print quality were observed between the two halves: the bottom part exhibited fewer defects and more consistent layer adhesion, while the top part showed visible layer defects and irregular surface finish.

Additionally, during removal from the print bed, the exterior top surfaces of both halves (the glued interface) were slightly torn. However, this superficial damage is not expected to affect the following mechanical or dosimetric measurements, as it occurred outside the functionally relevant regions.

Despite the described difficulties, the completed TPU phantom was successfully printed for subsequent evaluation.

3.1.6 Post-processing

The PLA phantom required no post-processing. The parts were ready to use directly after removal from the printer, with clean surface finish and accurate fit for the applicator and scintillator. Channels were tested by inserting the applicator and scintillator directly, confirming that tolerances were acceptable without sanding or mechanical correction.

Post-processing for the TPU phantom was similarly minimal. After printing, the only required step was careful removal from the print bed, which had been manually glued to prevent warping during fabrication. No trimming or sanding was necessary, and the channel geometries were sufficiently accurate for insertion testing. While some minor surface imperfections and superficial tearing occurred at the base layer during removal, these did not interfere with the phantom's intended function or subsequent evaluation.

This structured approach highlights how the choice of material, rigid versus flexible, impacts nearly every stage of the development cycle, from CAD modeling through to final application.

3.2 CT-based dimensional validation

To assess the geometric fidelity of the printed phantoms, CT imaging was used to compare physical dimensions against the original CAD model. Both the PLA and TPU phantoms were scanned using clinical CT scanners under standardized imaging protocols.

For the PLA phantom, imaging was performed with a slice thickness of 1.0 mm and an in-plane voxel size of 0.586 × 0.586 mm. For the TPU phantom, higher resolution imaging was achieved with a 0.5 mm slice thickness and a voxel size of 0.293 × 0.293 mm. These differences reflected the need for higher spatial accuracy when analyzing the more deformable TPU material.

The dimensional analysis was conducted using 3D Slicer, a widely used open-source software tool for medical image segmentation and measurement. Using its caliper tool, critical geometric features of the phantoms were measured in three planes and compared to their digital design specifications. Key parameters included the channel diameters for the applicator and scintillator, the spacing between these channels, and the tip-to-tip distance from source to detector. Measurements were repeated three times to ensure consistency.

In addition to direct dimensional comparison, the analysis also considered the influence of CT resolution and blooming artifacts, particularly around dense regions such as the applicator channel. These artifacts sometimes obscured true channel boundaries, particularly in the PLA phantom. Therefore, any submillimeter discrepancies were interpreted within the context of the scanner's resolution threshold (estimated at 0.7–1.0 mm for PLA and 0.4–0.6 mm for TPU).

A deviation was considered acceptable if it remained below the estimated resolution limit of the CT scanner. Any dimensional discrepancy exceeding this threshold would constitute a geometric failure and warrant model redesign or reprint.

This method provided a non-destructive and spatially resolved way to assess whether the physical phantom accurately reflected the intended design, and established confidence in subsequent dosimetric measurements performed using the same structures.

3.3 Dosimetric testing setup

3.3.1 Plastic scintillator dosimetry

Plastic scintillator detectors were used to perform real-time point-dose measurements within the phantoms. The system consisted of a plastic scintillating element connected to an optical fiber and read out by a photodiode. Prior to experimental use, the system was calibrated using a standardized HDR brachytherapy source under TG-43 formalism assumptions [80].

Measurements were performed in two irradiation geometries: one with eleven dwell positions spaced 2 mm apart and one with five dwell positions spaced 5 mm apart. Dwell times were standardized at 10 seconds per position. The source activity was recorded for each session and used to calculate the expected dose for comparison.

The acquisition frequency of the scintillator system was varied (5 Hz, 10 Hz, 14 Hz) to evaluate temporal response and dose integration stability. The phantom orientation and applicator placement were kept fixed using indexed setup marks to ensure geometric reproducibility between measurements.

Repeat measurements were performed to assess reproducibility and the deviation between calculated and measured doses was used to evaluate dosimetric agreement. Agreement between measured and calculated dose was considered acceptable if deviations remained within ±5% for central dwell positions and ±10% for peripheral positions. Values exceeding these thresholds were flagged for further investigation.

3.3.2 Film dosimetry

Gafchromic™ EBT3 radiochromic film was used to capture 2D dose distributions in the TPU phantom. The film was cut to fit a dedicated planar cavity designed into the phantom, ensuring consistent alignment with the source and detector channels.

Films were irradiated using the same HDR source and dwell time settings used in the scintillator measurements. After irradiation, films were stored in light-protected conditions for at least 96 hours to allow polymerization to stabilize. They were then scanned using an Epson® Expression 12000XL flatbed scanner under consistent settings.

A calibration curve was established by irradiating reference film strips to known doses using a clinical linear accelerator. Optical density values were extracted from a central region of interest on each strip and fitted to a polynomial curve, which was subsequently used to convert film intensity values to absorbed dose.

Film data were analyzed using FilmQA Pro™ (Ashland™), a commercial software designed for quantitative film dosimetry. The software enabled both absolute dose conversion and gamma analysis. Dose profiles were extracted from regions of interest located 1 cm from the applicator path to match the reference position of the plastic scintillator.

The primary goal of film dosimetry in this study was to evaluate the performance of the TPU phantom by providing a high-resolution, planar dose distribution that could be compared directly to TG-43 calculations. This allowed for a spatially resolved assessment of how well the TPU phantom replicated dose patterns under HDR conditions, especially in light of its known departure from water equivalence.

In addition to assessing phantom performance, the film dosimetry data also provided complementary validation alongside plastic scintillator measurements. Taken together, these techniques supported a more complete and robust QA strategy by enabling both point-wise and planar verification of delivered dose in 3D-printed HDR brachytherapy phantoms.

4. Results

4.1 CT-based dimensional validation

The CT scans revealed that both the PLA and TPU phantoms closely matched their respective CAD models. Key dimensional features, including channel diameters and source-to-detector distances, remained within acceptable limits when compared to the original design. For the PLA phantom, measured values differed by no more than ±0.3 mm, while the TPU phantom exhibited slightly larger variability due to its flexible material properties, which can be seen in Table 7 and 8.

Table 7: PLA phantom CT measurements

Feature	**Measured (mm)**	**CAD (mm)**	**Notes**
Applicator channel air gap	2.001	0.0	Affected by blooming artifact
Applicator channel length	—	105.3	Blooming affects measurement significantly
Applicator channel width × height	—	3.9 × 3.95	Blooming affects measurement significantly
Scintillator channel air gap	0.45	0.0	
Scintillator length	114.9	115.03	
Scintillator width × height	5.416 × 5.209	5.4 × 5.2	
Applicator–scintillator Spacing	10.01	10.00	
Tip-to-tip distance	17.63	17.69	

Table 8: TPU phantom CT measurements

Feature	**Measured (mm)**	**CAD (mm)**	**Notes**
Applicator channel air gap	1.024	0.0	Affected by blooming artifact
Applicator channel length	—	105	Blooming affects measurement significantly
Applicator channel width × height	—	3.7 × 3.95	Blooming affects measurement significantly
Scintillator channel air gap	0.289	0.0	(measured on 1 mm slice thickness)
Scintillator length	114.5	115	
Scintillator width × height	5.590 × 5.180	5.4 × 5.2	
Applicator–scintillator spacing	9.832	10.00	
Tip-to-tip distance	17.96	17.69	(measured on 1 mm slice thickness)

Blooming artifacts were observed in both phantoms, particularly around dense structures such as the applicator channel in the PLA model. These artifacts influenced apparent diameters and introduced uncertainty in edge detection. Despite this, all deviations remained within the resolution threshold of the imaging systems (0.7–1.0 mm for PLA, 0.4–0.6 mm for TPU) (Table 9), indicating satisfactory geometric accuracy. The measurements confirmed that no deviations exceeded what could be resolved by the CT scanner, supporting the validity of subsequent dosimetric comparisons.

Table 9: Imaging protocol and resolution

Phantom	**Slice Thickness (mm)**	**Voxel Size (mm)**	**Estimated Resolution (mm)**
PLA Phantom	1.0	0.586 × 0.586 × 1.0	0.7–1.0
TPU Phantom	0.5	0.293 × 0.293 × 0.5	0.4–0.6

4.2 Applicator insertion testing

Both PLA and TPU phantoms successfully accommodated the commercial BT applicator (Figure 7 and 8). The PLA phantom showed a consistent fit with minor air gaps, while the TPU phantom demonstrated improved surface conformity due to its elastic properties, allowing tighter channel engagement. Manual insertion tests confirmed that the applicator could be positioned reproducibly and without damage in both materials, with TPU offering slightly better channel-to-surface contact.

Figure 7: PLA phantom with applicator inside

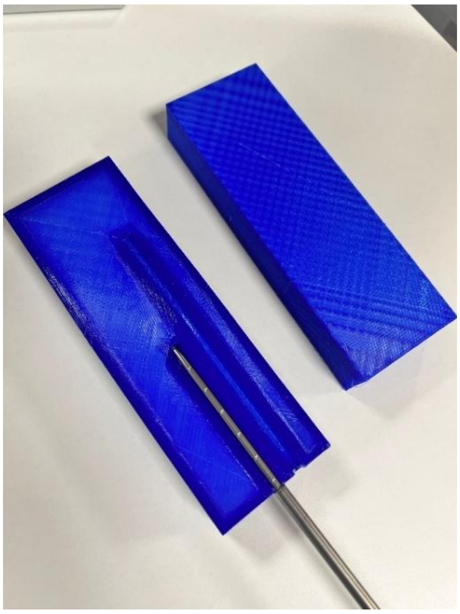

Figure 8: TPU phantom with applicator inside

4.3 CT-based density validation

To evaluate the radiological water equivalence of the phantom materials, CT imaging was used to assess HU in selected segments of both the PLA and TPU phantoms. Multiple regions of interest (ROIs) were segmented from CT images,and HU values were extracted using dedicated analysis software (Figure 9 to 12).

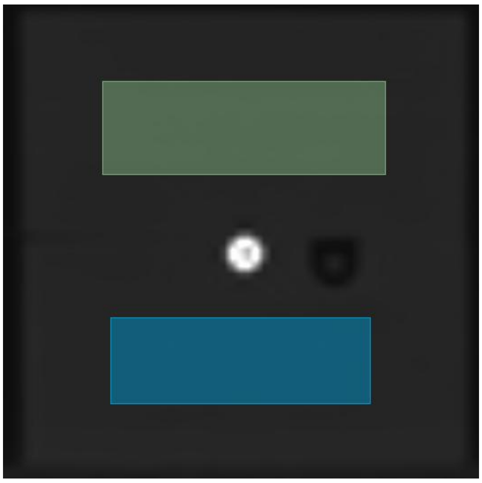

Figure 9: Axial image of PLA phantom with segments

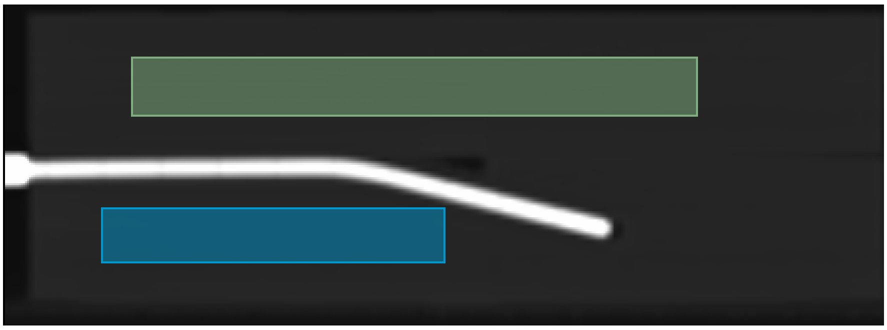

Figure 10: Sagittal image of PLA phantom with segments

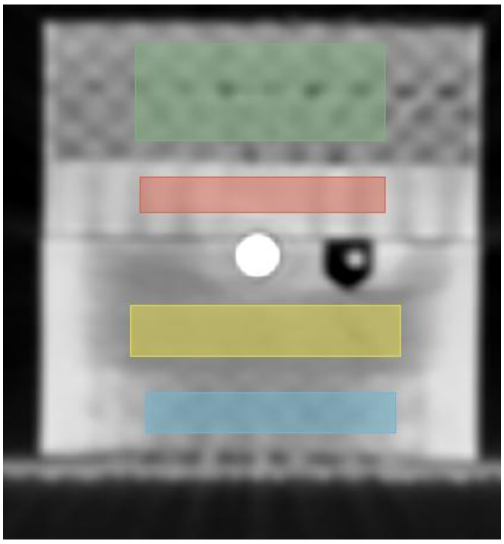

Figure 11: Axial image of TPU phantom with segments

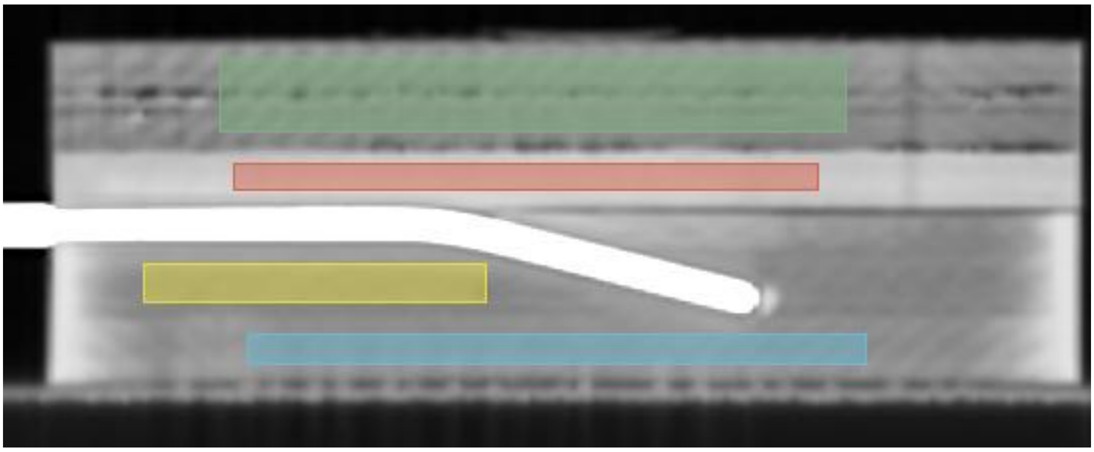

Figure 12: Sagittal image of TPU phantom with segments

For PLA, the top and bottom segments demonstrated mean HU values of –63 and –49, respectively, indicating reasonably close approximation to water (HU = 0) and confirming moderate water equivalence. In contrast, the TPU phantom showed significant variability across regions, with mean HU values ranging from –327 to +11.

These differences in density and internal structure are relevant for dosimetric comparison with TG-43 calculations, which assume a homogeneous water-equivalent environment. The full results of the CT-based HU analysis are summarized in Tables 10 and 11.

Table 10: Analysis of PLA phantom density

No.	**Segment**	**Minimum [HU]**	**Maximum [HU]**	**Mean [HU]**	**Std dev. [HU]**
1	PLA Top	-115	-18	-63.2106	10.6702
2	PLA Bottom	-101	12	-48.6466	14.2816

Table 11: Analysis of TPU phantom density

No.	**Segment**	**Minimum [HU]**	**Maximum [HU]**	**Mean [HU]**	**Std dev. [HU]**
1	TPU Top less dense	-832	-57	-327.268	70.3456
2	TPU Top more dense	-153	111	11.115	40.0936
3	TPU Bottom homogeneous	-436	-188	-305.371	25.6091
4	TPU Bottom grid like	-374	-26	-253.592	55.1347

4.4 Plastic scintillator dosimetry

Dose measurements obtained using the plastic scintillator in the PLA phantom showed good agreement with TPS calculations based on TG-43 calculations. Table 12 depicts the comparison between scintillator measurement and TG-43 calculation. In the five-dwell setup (Figure 13), deviations ranged from 1.72% to 9.96%, with the largest discrepancies occurring at distal dwell positions (Table 13). The eleven-dwell setup (Figure 14) displayed a similar pattern, with differences from 0,07% to 8,52% depending on dwell location (Table 14).

Table 12: PLA comparison between scintillator measurement and TG-43 calculation

Trial	**Measured Dose [Gy]**	**TG-43 calculation [Gy]**	**Difference [%]**
5 dwell	1.03273	1.050	1.644762
11 dwell	2.25314	2.268	0.655203

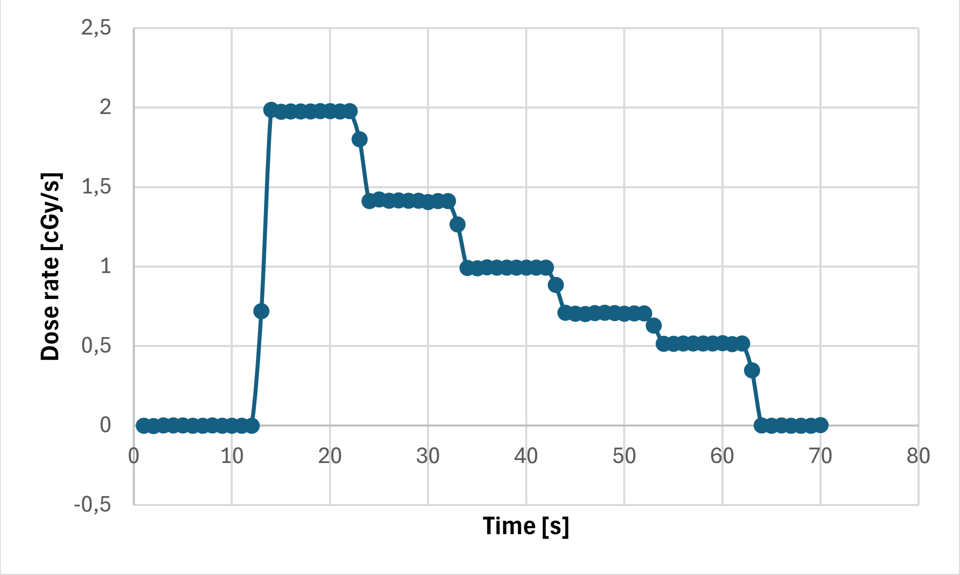

Figure 13: PLA 5 dwell scintillator graph

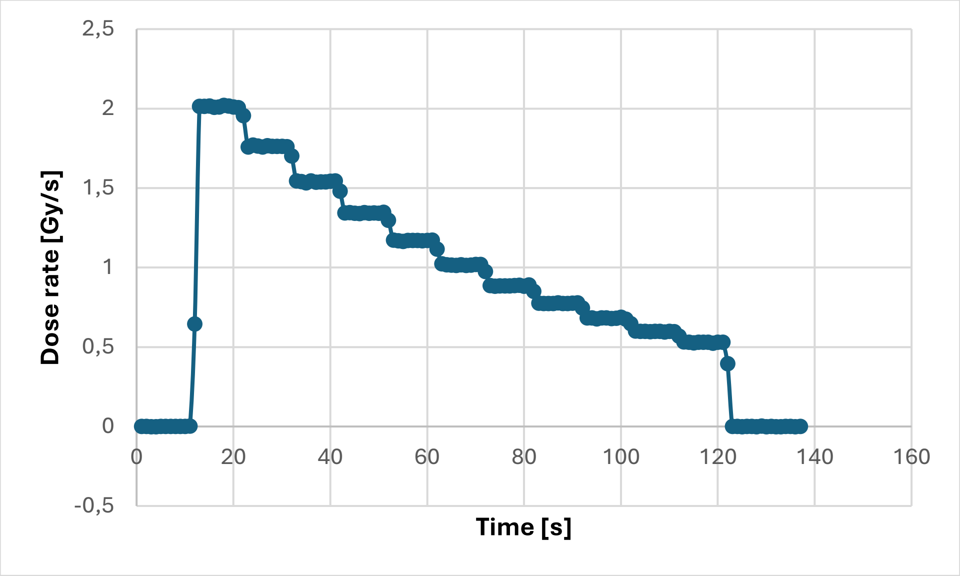

Figure 14: PLA 11 dwell scintillator graph

Figures 13 and 14 clearly illustrate the dose rate measured during the procedure, highlighting the effectiveness of the scintillator's real-time readout capability. The step-like pattern in the graphs, marked by distinct drops in dose rate, indicates transitions between individual dwell positions.

Table 13: Contributions for the PLA 5 dwell positions

Dwell position	**Scintillator measurement [cGy]**	**TG-43 dose [cGy]**	**Deviation [%]**	**Scintillator dwell contribution [%]**	**TG-43 dwell contribution [%]**
1	37.39655	36.2	3.31	36.2	34.48
2	25.74915	26.2	1.72	26.2	24.95
3	18.07732	18.7	3.33	18.7	17.81
4	12.85796	13.7	6.15	13.7	13.05
5	9.183839	10.2	9.96	10.2	9.71
Total	**103.2648**	**105**		**100.00**	**100.00**

Table 14: Contributions for the PLA 11 dwell positions

Dwell position	**Scintillator measurement [cGy]**	**TG-43 dose [cGy]**	**Deviation [%]**	**Scintillator dwell contribution [%]**	**TG-43 dwell contribution [%]**
1	37.89152	36.1	4,96	16.82	15.92
2	32.13414	31.9	0,73	14.26	14.07
3	28.07426	28	0,27	12.46	12.35
4	24.4838	24.5	0,07	10.87	10.80
5	21.29276	21.5	0,96	9.45	9.48
6	18.52325	18.8	1,47	8.22	8.29
7	16.13284	16.6	2,81	7.16	7.32
8	14.11602	14.6	3,31	6.26	6.44
9	12.3909	13	4,69	5.50	5.73
10	10.87638	11.5	5,42	4.83	5.07
11	9.42261	10.3	8,52	4.18	4.54
Total	**225.3385**	**226.8**		**100.00**	**100.00**

To complement the PLA phantom testing, the TPU phantom was evaluated under extended measurement conditions. An initial calibration was performed using a single dwell position irradiated for 50 seconds, which was scaled to 89.353 seconds to compensate for the lower source strength of 5.596 Ci. This yielded a dose of 1.846 Gy and was repeated three times, with the following results (Table 15).

Table 15: Calibration results TPU phantom

Trial	Measured dose [Gy]
1	1.88695
2	1.88042
3	1.86776

Next, the TPU phantom underwent the same 11-dwell position protocol used previously in PLA testing, with 2 mm inter-dwell spacing and 10 seconds per dwell. Due to reduced source activity, the total time was scaled from 110 seconds to 196.581 seconds. The measured and calculated dose values are shown below in table 16.

Table 16: TPU 11 dwell position comparison between scintillator and TG-43

Trial	Measured dose [Gy]	TG-43 calculation [Gy]	Difference [%]
1	2.35180	2.384	-1.35%
2	2.30238	2.384	-3.43%
3	2.31950	2.384	-2.70%

To investigate the influence of measurement frequency on signal fidelity, the 11-dwell protocol was repeated with varied acquisition rates. Results are summarized below in Table 17.

Table 17: Comparison of different measurement frequencies

Frequency [Hz]	Measured dose [Gy]
5	2.33578
10	2.34659
14	2.33727

These results indicate that increased temporal resolution does not negatively affect scintillator performance or dose integration accuracy.

Finally, the TPU phantom underwent the same 5-dwell position protocol as the PLA phantom, with 5 mm spacing, 10 seconds dwell time, and a 14 Hz acquisition rate. Time was scaled from 50 to 89.355 seconds. The acquired and calculated dose values are shown in Table 18.

Table 18: Dwell position comparing scintillator to TG-43

Trial	Measured Dose [Gy]	TG-43 calculation [Gy]	Difference [%]
1	1.08731	1.103	-1.42%
2	1.08660	1.103	-1.49%
3	1.09221	1.103	-0.98%

The contribution of each dwell position to total measured dose under the 11- (Figure 15) and 5-dwell (Figure 16) protocol in the TPU phantom is outlined below in Table 19 and Table 20.

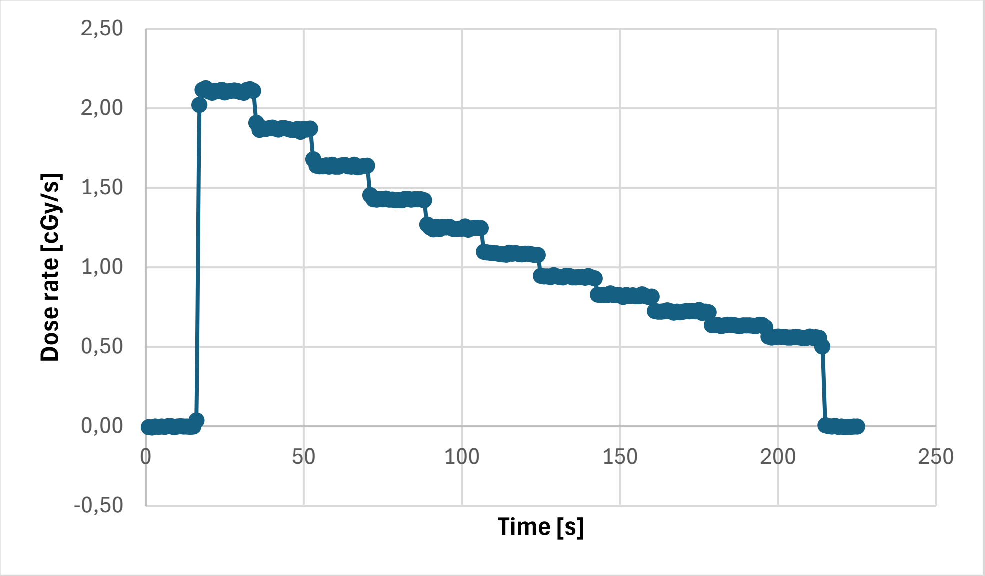

Figure 15: TPU 11 dwell scintillator graph

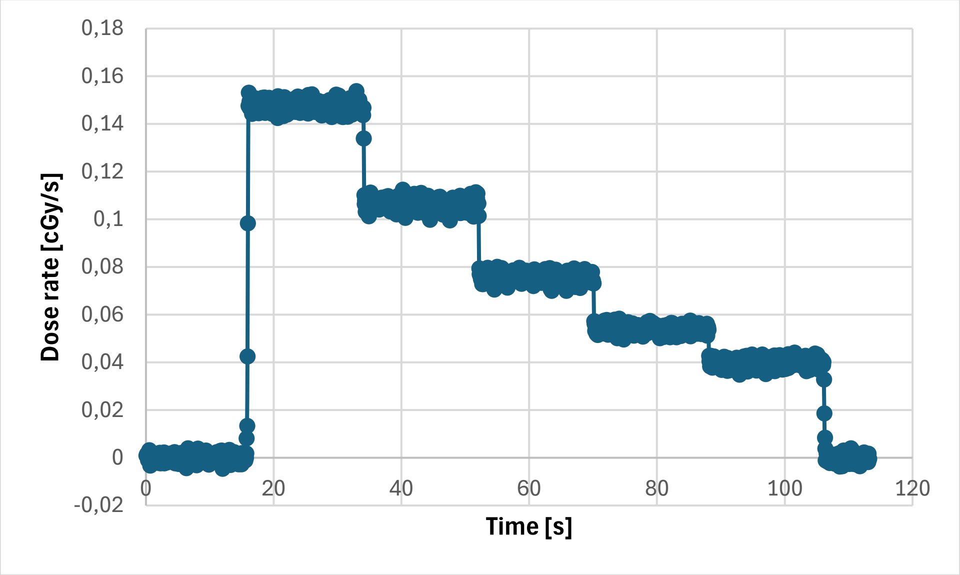

Figure 16: TPU 5 dwell scintillator graph

Table 19: TPU contributions for the 11 dwell positions

Dwell position	**Scintillator measurement [cGy]**	**TG-43 dose [cGy]**	**Deviation [%]**	**Scintillator dwell contribution [%]**	**TG-43 dwell contribution [%]**
1	37.947183	36.80	3.12	16.13	15.61
2	33.715688	32.9	2.48	14.33	13.95
3	29.53143	29.1	1.48	12.55	12.34
4	25.724855	25.6	0.49	10.94	10.86
5	22.479865	22.5	0.09	9.56	9.54
6	19.561049	19.7	0.71	8.32	8.35
7	16.945054	17.4	2.61	7.20	7.38
8	14.830021	15.3	3.07	6.30	6.49
9	13.01092	13.6	4.33	5.53	5.77
10	11.432175	12.1	5.52	4.86	5.13
11	10.03972	10.8	7.04	4.27	4.58
Total	**235.22**	**235.80**		**100.0**	**100.0**

Table 20: TPU contributions for the 5 dwell positions

Dwell position	**Scintillator measurement [cGy]**	**TG-43 dose [cGy]**	**Deviation [%]**	**Scintillator dwell contribution [%]**	**TG-43 dwell contribution [%]**
1	37.88335	37.5	1.02	34.68	33.78
2	27.62667	27.9	0.98	25.29	25.14
3	19.53701	20.1	2.80	17.89	18.11
4	13.97105	14.6	4.31	12.79	13.15
5	10.21189	10.9	6.31	9.35	9.82
Total	**109.23**	**111.00**		**100.0**	**100.0**

4.5 Film dosimetry in the TPU phantom

The EBT3 film analysis provided high-resolution, 2D dose distributions for both 5- and 11-dwell irradiation setups in the TPU phantom. These maps displayed concentric isodose contours with steep gradients, consistent with the expected geometry of an Ir-192 HDR-BT source.

Figure 17 shows a 3D graph comparing the dose distributions for both setups, where the smaller peak represents the 5-dwell irradiation and the larger peak corresponds to the 11-dwell setup. Figure 18 further illustrates the spatial distribution with a 2D pseudo-color heatmap, confirming symmetry and the location of dose maxima adjacent to the source path.

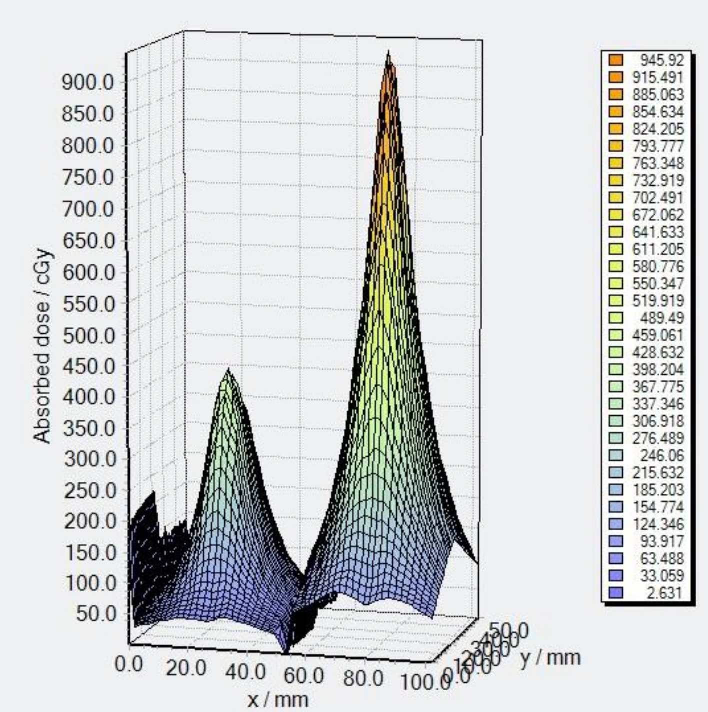

Figure 17: 3D graph of EBT3 film measurement of 5 and 11 dwell positions

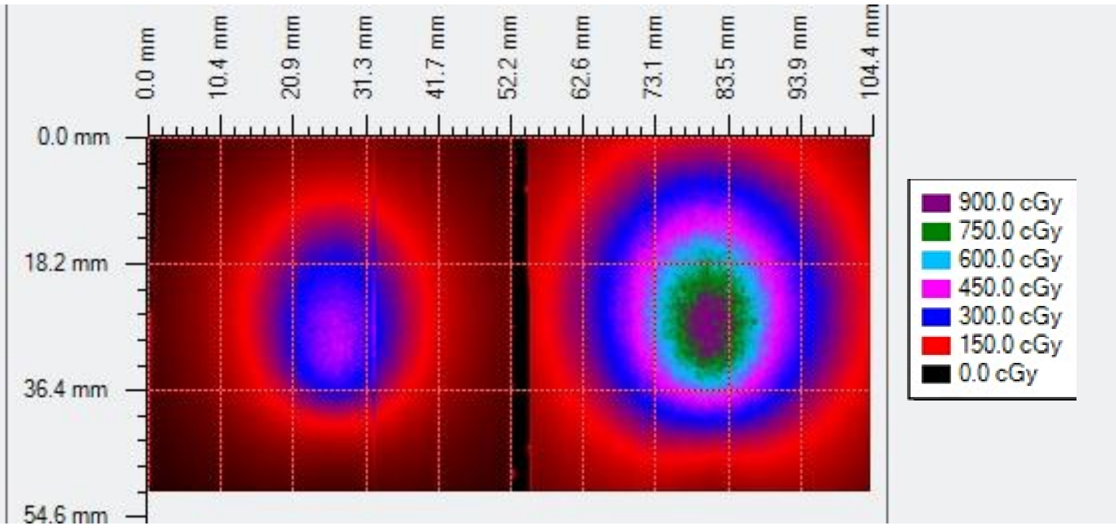

Figure 18: Absorbed dose distribution for the 5 and 11 dwell positions

Quantitative comparison with TG-43 calculations showed a consistent difference in measured dose. As presented in Table 13, the film-measured dose was significantly higher than the dose calculated by TG-43 at a fixed measurement distance of 1 cm from the source. The measured doses were approximately 88% to 94% greater than the calculated values (Table 21).

Table 21: Comparison between EBT3 film and TG-43

Dose measured on film [cGy]	**Dose calculation by TG-43 [cGy]**	**Difference [%]**
205.1315	109.221	187.8132
449.5682	231.95	193.8212

CT scans of the TPU phantom showed local regions with HU values as low as –400, indicating reduced physical density relative to water. This information provides context for differences in measured versus calculated dose values, particularly given that TG-43 is based on uniform water-equivalent assumptions.

5. Discussion

5.1 Dimensional accuracy from CT validation

The CT-based dimensional validation confirmed that both PLA and TPU phantoms were manufactured with high geometric fidelity relative to their CAD models. Most deviations were within the resolution threshold of the imaging systems used, which was set as the acceptance criterion for dimensional accuracy (0.7–1.0 mm for PLA and 0.4–0.6 mm for TPU). No measurements exceeded these thresholds, indicating compliance with the pass criteria. This result validates the 3D printing approach and confirms the feasibility of using FDM-printed phantoms in QA workflows where dimensional accuracy is critical.

However, blooming artifacts near high-density regions, particularly around the applicator channel, introduced some uncertainty in edge delineation. These artifacts highlight a limitation of CT imaging when high-density materials, such as metal or dense applicator components, are present within the phantom. This is primarily due to partial volume effects and voxel averaging, where a small inclusion of high-attenuation material within a voxel can significantly skew the calculated HU. In contrast, low-density regions such as air are less affected.

Since direct physical measurement of internal phantom geometries is impractical, one pragmatic approach is to perform CT imaging of the phantom with the applicator removed. This allows accurate measurement of the applicator channel dimensions without the confounding effects of metal artifacts. However, this method cannot capture how well the applicator fits within the channel such as the presence of air gaps, which may influence dose distribution. A more comprehensive approach would involve acquiring a combination of CT scans with and without the applicator inserted. For studies requiring enhanced spatial resolution, high-resolution imaging modalities such as micro-CT may also be considered, although their practical use may be limited by scanning volume and equipment availability. Due to time constraints in this study, only CT imaging with the applicator in place was acquired. The possibility of scanning the phantom without the applicator to isolate channel dimensions was identified late in the research process, shortly before the final deadline. As a result, there was insufficient time to implement this additional imaging step.

5.2 Applicator insertion performance

Both phantom materials allowed successful applicator insertion, though their mechanical performance differed. PLA exhibited rigid stability but was prone to small air gaps due to its stiffness and low compliance, whereas TPU's flexibility enabled improved conformity around the applicator, leading to better surface contact. However, insertion into the TPU phantom was more difficult due to the tighter channel tolerances and reduced clearance. This challenge was mitigated by the use of ultrasound gel as a lubricant. The gel, having a density close to that of water, not only improved insertion ease but also better simulated clinical insertion conditions and reduced friction. These mechanical differences may have implications for long-term durability or repeated use in clinical QA, where insertion consistency must be maintained.

5.3 Density validation

The CT-based density validation revealed notable differences in the structural uniformity and radiological equivalence of the PLA and TPU phantoms. These characteristics have critical implications for the accuracy and applicability of dose calculations, particularly when benchmarked against algorithms such as TG-43 that assume a homogenous water-equivalent environment.

The PLA phantom displayed a rectilinear internal structure that was both visually and quantitatively consistent. CT measurements demonstrated that the PLA material had HU values slightly below that of water, yet still within a range that could be considered acceptable for approximate water equivalence. The consistency of these HU values suggests that the PLA phantom possessed uniform density throughout its volume, contributing to reliable and predictable dosimetric behavior. With slight underdensity being the primary deviation, it is reasonable to conclude that a modest increase in infill percentage during the printing process could further improve the PLA phantom's water equivalence.

In contrast, the TPU phantom exhibited a high degree of heterogeneity. The CT scans revealed that the top half of the phantom contained two visibly distinct regions: one with a grid-like low-density structure wherein some areas as low as –832 HU, and another with a denser, more solid pattern. The bottom section also demonstrated mixed characteristics, including a homogeneous but low-density region and another grid-like portion with significantly reduced HU values. These variations were compounded by air gaps and minor structural defects, which likely resulted from the challenges inherent in printing flexible materials using FDM techniques. Such inconsistencies compromise both geometric reproducibility and radiological stability, making accurate dose modeling more difficult.

The presence of very low-density zones and structural imperfections in the TPU phantom not only reduced its fidelity as a water-equivalent model but also likely contributed to the pronounced discrepancies observed between measured and TG-43-calculated dose values. These observations highlight the limitations of applying simplified, homogenous models to phantoms with significant internal heterogeneity.

To improve the quality of future TPU-based phantoms, several strategies could be considered. First, further optimization of FDM printing parameters, including infill density, extrusion temperature, and print speed, may help minimize internal variation. Second, reprinting until CT or post-processing analysis confirms the absence of internal defects would enhance material uniformity. Third, if reproducible homogeneity cannot be reliably achieved with current materials, exploring alternative flexible filaments with improved mechanical and radiological properties may be necessary.

Despite recognizing these avenues for improvement, they were not pursued in the current study due to practical constraints. The production of the TPU phantom required approximately 125 hours of printing, and the model used in the final evaluation was already the second iteration. Given the limited time remaining for dosimetric testing and analysis, as well as the higher material cost associated with TPU, a third print was deemed unfeasible. Consequently, the existing phantom was used for all subsequent measurements, and its limitations were taken into account in the interpretation of results.

5.4 Plastic scintillator dose measurements

The absolute dose measurements for both PLA and TPU phantoms remained around 1% of expected values in calibration tests. This high level of agreement suggests that the system calibration, including scintillator response normalization, phantom scattering conditions, and material properties, was both effective and robust. The low variability observed across different acquisition frequencies further supports the overall stability of the experimental setup. That such consistency was achieved in the TPU phantom, despite its non-water-equivalent composition and internal inhomogeneities, underscores the surprising reliability of its geometric and mechanical design in enabling reproducible measurements. However, it should be noted that this result reflects the effectiveness of calibration and experimental control, and not the inherent water-equivalence or dosimetric accuracy of the phantom material itself, as those material-specific effects were normalized during the calibration process.

Scintillator-based dose measurements performed in the PLA phantom revealed deviations from TG-43 dose calculations ranging from 1.72% to 9.96% in the 5-dwell setup and from 0.07% to 8.52% in the 11-dwell setup. All dwell positions remained within the ±10% threshold, satisfying the predefined pass criteria. These results indicate that the PLA phantom, which exhibited better water equivalence, provided dose measurements that aligned reasonably well with the TG-43 model, though some values approached the upper limit of acceptability.

The TPU phantom demonstrated more consistent and slightly lower deviations, with dose differences ranging from 0.98% to 6.31% in the 5-dwell protocol and from 0.09% to 7.04% in the 11-dwell protocol. While these values also fell within the pass thresholds, it's important to note that the TPU phantom was not water-equivalent, with CT measurements revealing HU as low as –400 in some regions. The smaller deviations may therefore reflect improved source-detector positioning stability due to the material's flexibility rather than an inherently more accurate dosimetric match to TG-43 assumptions.

The observed improvement in consistency for the TPU phantom may be attributed to several contributing factors. First, the TPU measurements were repeated multiple times, whereas the PLA measurements were performed only once. This increased sampling likely enabled a more accurate and representative comparison to TG-43 dose calculations. Second, the TPU datasets were acquired at higher sampling frequencies of 5 Hz, 10 Hz, and 14 Hz ,which allowed for finer temporal resolution and more precise attribution of dose to individual dwell positions. Lastly, the TPU phantom featured smaller margins around the applicator channel, which may have contributed to greater positional stability and setup consistency. This mechanical advantage likely improved source-to-detector alignment, leading to more reproducible measurements and ultimately smaller deviations from the TG-43 model.

These outcomes confirm the utility of plastic scintillator dosimetry for HDR QA and suggest that while TPU may offer mechanical advantages in reproducibility, PLA's material composition provides a more accurate dosimetric match when comparing to TG-43-based planning.

5.5 Film dosimetry and comparison with TG-43

Film dosimetry was primarily employed to assess the dosimetric behavior of the TPU phantom and provide high-resolution, planar dose data for comparison against TG-43 calculations. The green channel was selected for analysis due to high dose levels near the film's exposure peak. However, given that the location of interest experienced lower dose levels, the red channel might have been more suitable, as it generally offers better sensitivity in clinical dose ranges.

The film-measured doses exceeded TG-43 calculations by 88–94%, a clear indication of non-water-equivalent behavior in the TPU phantom. This result aligns with CT-based density evaluations, which showed significant radiological heterogeneity, including regions with HU as low as –400. These deviations illustrate how strongly the lack of water equivalence influences dose deposition and underscore the limitations of TG-43 in such materials.

Possible improvements include using a more water-equivalent phantom or refining the current TPU printing method to eliminate density inconsistencies. Additionally, film dosimetry could have been extended to the PLA phantom for comparison, as its closer approximation to water might result in improved agreement with TG-43. Moreover, incorporating dose calculation algorithms based on TG-186 (such as model-based dose calculation algorithms) would allow more meaningful comparisons in heterogeneous materials, even if perfect water equivalence cannot be achieved.

6. Conclusion

This study evaluated the feasibility, accuracy, and limitations of two 3D-printed phantoms, in PLA and TPU, for use in HDR-BT QA. Through dimensional validation, CT-based density analysis, mechanical insertion testing, and two independent dosimetric methods (plastic scintillator and film), both materials were critically assessed against predefined acceptance criteria and compared to TG-43 reference calculations.

The PLA phantom demonstrated strong dimensional fidelity and consistent internal structure, with HU values slightly below water, suggesting reasonable water equivalence. These properties translated into acceptable dose agreement in plastic scintillator measurements and would likely have shown similar consistency in film dosimetry had it been tested. TPU, while less water-equivalent and more structurally heterogeneous, showed mechanical advantages such as improved conformity and insertion stability, which likely contributed to its reproducibility and lower variability in scintillator-based dosimetry.

CT-based density validation revealed significant material-dependent differences in radiological properties, with PLA exhibiting more uniform and water-like attenuation characteristics, while TPU presented a complex internal structure with very low-density regions and printing-related defects. These disparities were reflected most strongly in the film dosimetry, where deviations from TG-43 exceeded 90%, emphasizing the inadequacy of applying water-based dosimetric models to non-uniform phantoms.

Despite these limitations, both materials fulfilled their intended purpose. PLA provided a geometrically and radiologically stable platform, while TPU enabled assessment of dosimetric deviations in non-water-equivalent conditions. Together, they offered complementary insights into the practical and theoretical boundaries of current QA practices.

Future improvements should include the refinement of print parameters for flexible materials, broader adoption of advanced dose calculation algorithms such as those aligned with TG-186, and expansion of comparative testing to include both phantom types in all dosimetric modalities. With continued optimization, 3D-printed phantoms hold strong potential to enhance QA workflows in BT, offering customizable, patient-specific solutions with meaningful clinical relevance.

References

[1] “Cervical cancer.” Accessed: Jun. 07, 2025. [Online]. Available: https://www.who.int/news-room/fact-sheets/detail/cervical-cancer

[2] H. Sung *et al.*, “Global Cancer Statistics 2020: GLOBOCAN Estimates of Incidence and Mortality Worldwide for 36 Cancers in 185 Countries,” *CA Cancer J Clin*, vol. 71, no. 3, pp. 209–249, May 2021, doi: 10.3322/CAAC.21660,.

[3] J. Ferlay *et al.*, “Cervix uteri,” Feb. 2024. Accessed: Mar. 07, 2025. [Online]. Available: https://gco.iarc.who.int/media/globocan/factsheets/cancers/23-cervix-uteri-fact-sheet.pdf

[4] A. Serarslan, D. Meydan, and R. E. Yildiz, “Radical Radiotherapy of Locally Advanced Cervix Uteri Carcinoma,” *Archives of Cancer Biology and Therapy,; Volume 2(Issue 1):8-14*, vol. Volume 2, no. Issue 1, pp. 8–14, Jun. 2021, doi: 10.33696/CANCERBIOLOGY.2.017.

[5] N. Eustace *et al.*, “Current Status and Future Directions of Image-Guided Adaptive Brachytherapy for Locally Advanced Cervical Cancer,” *Cancers 2024, Vol. 16, Page 1031*, vol. 16, no. 5, p. 1031, Mar. 2024, doi: 10.3390/CANCERS16051031.

[6] S. L. Richardson *et al.*, “AAPM medical physics practice guideline 13.a: HDR brachytherapy, part A,” *J Appl Clin Med Phys*, vol. 24, no. 3, p. e13829, Mar. 2023, doi: 10.1002/ACM2.13829.

[7] C. Kirisits *et al.*, “Review of clinical brachytherapy uncertainties: Analysis guidelines of GEC-ESTRO and the AAPM,” *Radiotherapy and Oncology*, vol. 110, no. 1, pp. 199–212, Jan. 2014, doi: 10.1016/J.RADONC.2013.11.002.

[8] J. Venselaar and J. Pérez-Calatayud, *A PRACTICAL GUIDE TO QUALITY CONTROL OF BRACHYTHERAPY EQUIPMENT EUROPEAN GUIDELINES FOR QUALITY ASSURANCE IN RADIOTHERAPY BOOKLET NO. 8*. 2004.

[9] T. Soror *et al.*, “Quality Assurance in Modern Gynecological HDR-Brachytherapy (Interventional Radiotherapy): Clinical Considerations and Comments,” *Cancers (Basel)*, vol. 13, no. 4, p. 912, Feb. 2021, doi: 10.3390/CANCERS13040912.

[10] M. Ashenafi, S. Jeong, J. N. Wancura, L. Gou, M. J. Webster, and D. Zheng, “A quick guide on implementing and quality assuring 3D printing in radiation oncology,” *J Appl Clin Med Phys*, vol. 24, no. 11, p. e14102, Nov. 2023, doi: 10.1002/ACM2.14102;WGROUP:STRING:PUBLICATION.

[11] F. J. Rybicki, J. M. Morris, and G. T. Grant, *3D Printing at Hospitals and Medical Centers A Practical Guide for Medical Professionals Second Edition*.

[12] J. Chino *et al.*, “Radiation Therapy for Cervical Cancer: Executive Summary of an ASTRO Clinical Practice Guideline,” *Pract Radiat Oncol*, vol. 10, no. 4, p. 220, Jul. 2020, doi: 10.1016/J.PRRO.2020.04.002.

[13] C. W. Williamson, H. C. Liu, J. Mayadev, and L. K. Mell, “Advances in External Beam Radiation Therapy and Brachytherapy for Cervical Cancer,” *Clin Oncol*, vol. 33, no. 9, pp. 567–578, Sep. 2021, doi: 10.1016/J.CLON.2021.06.012.

[14] M. McCormack *et al.*, “Induction chemotherapy followed by standard chemoradiotherapy versus standard chemoradiotherapy alone in patients with locally advanced cervical cancer (GCIG INTERLACE): an international, multicentre, randomised phase 3 trial.,” *Lancet*, vol. 404, no. 10462, pp. 1525–1535, Oct. 2024, doi: 10.1016/S0140-6736(24)01438-7.

[15] Z. Végváry *et al.*, “MRI-based image-guided adaptive brachytherapy for locally advanced cervical cancer in clinical routine: a single-institution experience,” *Pathology and Oncology Research*, vol. 31, p. 1612077, 2025, doi: 10.3389/PORE.2025.1612077.

[16] K. Wang, J. Wang, and P. Jiang, “High-Dose-Rate Three-Dimensional Image-Guided Adaptive Brachytherapy (3D IGABT) for Locally Advanced Cervical Cancer (LACC): A Narrative Review on Imaging Modality and Clinical Evidence,” *Current Oncology 2024, Vol. 31, Pages 50-65*, vol. 31, no. 1, pp. 50–65, Dec. 2023, doi: 10.3390/CURRONCOL31010004.

[17] H. Liu *et al.*, “Review of cone beam computed tomography based online adaptive radiotherapy: current trend and future direction,” *Radiation Oncology*, vol. 18, no. 1, pp. 1–12, Dec. 2023, doi: 10.1186/S13014-023-02340-2/METRICS.

[18] C. E. Shelley, L. H. Barraclough, C. L. Nelder, S. J. Otter, and A. J. Stewart, “Adaptive Radiotherapy in the Management of Cervical Cancer: Review of Strategies and Clinical Implementation,” *Clin Oncol*, vol. 33, no. 9, pp. 579–590, Sep. 2021, doi: 10.1016/J.CLON.2021.06.007.

[19] G. Wang *et al.*, “Daily Online Adaptive Radiation Therapy of Postoperative Endometrial and Cervical Cancer With PTV Margin Reduction to 5 mm: Dosimetric Outcomes, Acute Toxicity, and First Clinical Experience,” *Adv Radiat Oncol*, vol. 9, no. 7, p. 101510, Jul. 2024, doi: 10.1016/J.ADRO.2024.101510.

[20] A. E. Silberstein *et al.*, “Cone-Beam Computed Tomography (CBCT)-Guided Adaptive Boost Radiotherapy for a Patient With Locally Advanced Cervical Cancer Ineligible for Brachytherapy,” *Cureus*, vol. 16, no. 8, Aug. 2024, doi: 10.7759/CUREUS.66218.

[21] C. E. Shelley *et al.*, “Implementing cone-beam computed tomography-guided online adaptive radiotherapy in cervical cancer,” *Clin Transl Radiat Oncol*, vol. 40, May 2023, doi: 10.1016/j.ctro.2023.100596.

[22] Y. Zhang *et al.*, “Prospects for daily online adaptive radiotherapy for cervical cancer: Auto-contouring evaluation and dosimetric outcomes,” *Radiation Oncology*, vol. 19, no. 1, pp. 1–10, Dec. 2024, doi: 10.1186/S13014-024-02398-6/TABLES/3.

[23] S. Y. Ryu *et al.*, “Randomized clinical trial of weekly vs. triweekly cisplatin-based chemotherapy concurrent with radiotherapy in the treatment of locally advanced cervical cancer,” *Int J Radiat Oncol Biol Phys*, vol. 81, no. 4, Nov. 2011, doi: 10.1016/j.ijrobp.2011.05.002.

[24] P. G. Rose *et al.*, “Concurrent Cisplatin-Based Radiotherapy and Chemotherapy for Locally Advanced Cervical Cancer,” *New England Journal of Medicine*, vol. 340, no. 15, pp. 1144–1153, Apr. 1999, doi: 10.1056/NEJM199904153401502/ASSET/77DD6054-CF6B-4038-94B0-8F4FEBE4BE2F/ASSETS/IMAGES/LARGE/NEJM199904153401502_T4.JPG.

[25] Z. Otty *et al.*, “Efficacy and tolerability of weekly low-dose cisplatin concurrent with radiotherapy in head and neck cancer patients,” *Asia Pac J Clin Oncol*, vol. 7, no. 3, pp. 287–292, Sep. 2011, doi: 10.1111/J.1743-7563.2011.01405.X,.

[26] R. P. Miller, R. K. Tadagavadi, G. Ramesh, and W. B. Reeves, “Mechanisms of Cisplatin Nephrotoxicity,” *Toxins (Basel)*, vol. 2, no. 11, p. 2490, Nov. 2010, doi: 10.3390/TOXINS2112490.

[27] R. Pötter *et al.*, “Recommendations from gynaecological (GYN) GEC ESTRO working group (II): Concepts and terms in 3D image-based treatment planning in cervix cancer brachytherapy - 3D dose volume parameters and aspects of 3D image-based anatomy, radiation physics,

radiobiology," *Radiotherapy and Oncology*, vol. 78, no. 1, pp. 67–77, Jan. 2006, doi: 10.1016/j.radonc.2005.11.014.

[28] F. Mignot *et al.*, "Comprehensive analysis of patient outcome after local recurrence of locally advanced cervical cancer treated with concomitant chemoradiation and image-guided adaptive brachytherapy," *Gynecol Oncol*, vol. 157, no. 3, pp. 644–648, Jun. 2020, doi: 10.1016/J.YGYNO.2020.03.006.

[29] R. Pötter *et al.*, "MRI-guided adaptive brachytherapy in locally advanced cervical cancer (EMBRACE-I): a multicentre prospective cohort study," *Lancet Oncol*, vol. 22, no. 4, pp. 538–547, Apr. 2021, doi: 10.1016/S1470-2045(20)30753-1.

[30] K. Tanderup *et al.*, "Image Guided Adaptive Brachytherapy in cervix cancer: A new paradigm changing clinical practice and outcome," *Radiotherapy and Oncology*, vol. 120, no. 3, pp. 365–369, Sep. 2016, doi: 10.1016/J.RADONC.2016.08.007,.

[31] A. Schernberg *et al.*, "Tumor Shrinkage During Chemoradiation in Locally Advanced Cervical Cancer Patients: Prognostic Significance, and Impact for Image-Guided Adaptive Brachytherapy," *Int J Radiat Oncol Biol Phys*, vol. 102, no. 2, pp. 362–372, Oct. 2018, doi: 10.1016/j.ijrobp.2018.06.014.

[32] P. Trnková *et al.*, "New inverse planning technology for image-guided cervical cancer brachytherapy: Description and evaluation within a clinical frame," *Radiotherapy and Oncology*, vol. 93, no. 2, pp. 331–340, Nov. 2009, doi: 10.1016/J.RADONC.2009.10.004.

[33] A. Sturdza *et al.*, "Image guided brachytherapy in locally advanced cervical cancer: Improved pelvic control and survival in RetroEMBRACE, a multicenter cohort study," *Radiotherapy and Oncology*, vol. 120, no. 3, pp. 428–433, Sep. 2016, doi: 10.1016/j.radonc.2016.03.011.

[34] L. T. Tan *et al.*, "Education and training for image-guided adaptive brachytherapy for cervix cancer—The (GEC)-ESTRO/EMBRACE perspective," *Brachytherapy*, vol. 19, no. 6, pp. 827–836, Nov. 2020, doi: 10.1016/j.brachy.2020.06.012.

[35] N. Bhatla *et al.*, "Revised FIGO staging for carcinoma of the cervix uteri," *International Journal of Gynecology and Obstetrics*, vol. 145, no. 1, pp. 129–135, Apr. 2019, doi: 10.1002/IJGO.12749,.

[36] S. I. Lee and M. Atri, "2018 FIGO staging system for uterine cervical cancer: Enter Cross-sectional Imaging," *Radiology*, vol. 292, no. 1, pp. 15–24, 2019, doi: 10.1148/RADIOL.2019190088.

[37] N. C. S. Mezger *et al.*, "NCCN guideline–concordant cancer care in sub-Saharan Africa: a population-based multicountry study of 5 cancers," *J Natl Cancer Inst*, vol. 117, no. 1, pp. 120–133, Jan. 2025, doi: 10.1093/JNCI/DJAE221.

[38] J. Li, H. Cao, K. Peng, R. Chen, and X. Sun, "Hydronephrosis in patients with cervical cancer: An improved stent-change therapy for ureteral obstruction Stent-change for ureteral obstruction in cervical cancer," *European Journal of Obstetrics and Gynecology and Reproductive Biology*, vol. 283, pp. 49–53, Apr. 2023, doi: 10.1016/j.ejogrb.2023.01.026.

[39] H. H. Chung *et al.*, "Role of magnetic resonance imaging and positron emission tomography/computed tomography in preoperative lymph node detection of uterine cervical cancer," *Am J Obstet Gynecol*, vol. 203, no. 2, pp. 156.e1-156.e5, 2010, doi: 10.1016/j.ajog.2010.02.041.

[40] E. A. Kidd, I. El Naqa, B. A. Siegel, F. Dehdashti, and P. W. Grigsby, “FDG-PET-based prognostic nomograms for locally advanced cervical cancer,” *Gynecol Oncol*, vol. 127, no. 1, p. 136, Oct. 2012, doi: 10.1016/J.YGYNO.2012.06.027.

[41] H. J. Choi, W. Ju, S. K. Myung, and Y. Kim, “Diagnostic performance of computer tomography, magnetic resonance imaging, and positron emission tomography or positron emission tomography/computer tomography for detection of metastatic lymph nodes in patients with cervical cancer: Meta-analysis,” *Cancer Sci*, vol. 101, no. 6, pp. 1471–1479, Jun. 2010, doi: 10.1111/J.1349-7006.2010.01532.X,.

[42] I. Ríos, I. Vásquez, E. Cuervo, Ó. Garzón, and J. Burbano, “Problems and solutions in IGRT for cervical cancer,” *Reports of Practical Oncology and Radiotherapy*, vol. 23, no. 6, pp. 517–527, Nov. 2018, doi: 10.1016/J.RPOR.2018.05.002.

[43] Y. Lakhman, E. A. Aherne, V. S. Jayaprakasam, S. Nougaret, and C. Reinhold, “Staging of Cervical Cancer: A Practical Approach Using MRI and FDG PET,” *American Journal of Roentgenology*, vol. 225, no. 5, pp. 633–648, Nov. 2023, doi: 10.2214/AJR.23.29003,.

[44] W. Wang, F. Q. Zhang, and K. Hu, “Weekly Image Guidance in Patients with Cervical Cancer Treated with Intensity Modulated Radiation Therapy: Results of a Large Cohort Study,” *International Journal of Radiation Oncology*Biology*Physics*, vol. 117, no. 2, p. e553, Oct. 2023, doi: 10.1016/j.ijrobp.2023.06.1860.

[45] W. Wang *et al.*, “Efficacy and toxicity of image-guided intensity-modulated radiation therapy combined with dose-escalated brachytherapy for stage IIB cervical cancer,” *Oncotarget*, vol. 8, no. 61, p. 102965, 2017, doi: 10.18632/ONCOTARGET.22434.

[46] B. Rai *et al.*, “Three-Dimensional Conformal Radiotherapy Versus Image-Guided Intensity Modulated External Beam Radiotherapy in Locally Advanced Cervical Cancer: A Phase III Randomized Control Study,” *Clin Oncol*, vol. 36, no. 11, pp. 728–737, Nov. 2024, doi: 10.1016/j.clon.2024.08.004.

[47] S. W. Chen *et al.*, “Concurrent weekly cisplatin plus external beam radiotherapy and high-dose rate brachytherapy for advanced cervical cancer: A control cohort comparison with radiation alone on treatment outcome and complications,” *Int J Radiat Oncol Biol Phys*, vol. 66, no. 5, pp. 1370–1377, Dec. 2006, doi: 10.1016/j.ijrobp.2006.07.004.

[48] K. Tanderup *et al.*, “Effect of tumor dose, volume and overall treatment time on local control after radiochemotherapy including MRI guided brachytherapy of locally advanced cervical cancer,” *Radiotherapy and Oncology*, vol. 120, no. 3, pp. 441–446, Sep. 2016, doi: 10.1016/j.radonc.2016.05.014.

[49] T. Girinsky *et al.*, “Overall treatment time in advanced cervical carcinomas: A critical parameter in treatment outcome,” *Int J Radiat Oncol Biol Phys*, vol. 27, no. 5, pp. 1051–1056, Dec. 1993, doi: 10.1016/0360-3016(93)90522-W,.

[50] G. A. Viani, G. B. Manta, E. J. Stefano, and L. I. De Fendi, “Brachytherapy for cervix cancer: Low-dose rate or high-dose rate brachytherapy - A meta-analysis of clinical trials,” *Journal of Experimental and Clinical Cancer Research*, vol. 28, no. 1, 2009, doi: 10.1186/1756-9966-28-47,.

[51] S. Nag *et al.*, “Proposed guidelines for image-based intracavitary brachytherapy for cervical carcinoma: Report from Image-Guided Brachytherapy Working Group,” *International Journal of Radiation Oncology*Biology*Physics*, vol. 60, no. 4, pp. 1160–1172, Nov. 2004, doi: 10.1016/J.IJROBP.2004.04.032.

[52] S. Nag, C. Orton, D. Young, and B. Erickson, "The American brachytherapy society survey of brachytherapy practice for carcinoma of the cervix in the United States," *Gynecol Oncol*, vol. 73, no. 1, pp. 111–118, 1999, doi: 10.1006/gyno.1998.5334.

[53] A. J. Lin *et al.*, "Concurrent chemoradiation for cervical cancer: Comparison of LDR and HDR brachytherapy," *Brachytherapy*, vol. 18, no. 3, pp. 353–360, May 2019, doi: 10.1016/j.brachy.2018.11.008.

[54] E. J. Hall and D. J. Brenner, "Pulsed dose-rate brachytherapy," *Radiotherapy and Oncology*, vol. 45, no. 1, pp. 1–2, 1997, doi: 10.1016/S0167-8140(97)00166-7.

[55] C. Charra-Brunaud *et al.*, "Impact of 3D image-based PDR brachytherapy on outcome of patients treated for cervix carcinoma in France: Results of the French STIC prospective study," *Radiotherapy and Oncology*, vol. 103, no. 3, pp. 305–313, Jun. 2012, doi: 10.1016/j.radonc.2012.04.007.

[56] Z. Tian, M. Zhang, B. Hrycushko, K. Albuquerque, S. B. Jiang, and X. Jia, "Monte Carlo dose calculations for high-dose-rate brachytherapy using GPU-accelerated processing," *Brachytherapy*, vol. 15, no. 3, pp. 387–398, May 2016, doi: 10.1016/J.BRACHY.2016.01.006.

[57] M. J. Rivard *et al.*, "Update of AAPM Task Group No. 43 Report: A revised AAPM protocol for brachytherapy dose calculations," *Med Phys*, vol. 31, no. 3, pp. 633–674, 2004, doi: 10.1118/1.1646040,.

[58] A. Kanani, A. Owrangi, M. Yazdi, A. Fatemi-Ardekani, and M. A. Mosleh-Shirazi, "Development of a multi-purpose quality control phantom for MRI-based treatment planning in high-dose-rate brachytherapy of cervical cancer," *J Contemp Brachytherapy*, vol. 15, no. 1, pp. 57–68, 2023, doi: 10.5114/JCB.2023.125014,.

[59] E. L. Boman, T. W. S. Satherley, N. Schleich, D. B. Paterson, L. Greig, and R. J. W. Louwe, "The validity of Acuros BV and TG-43 for high-dose-rate brachytherapy superficial mold treatments," *Brachytherapy*, vol. 16, no. 6, pp. 1280–1288, Nov. 2017, doi: 10.1016/j.brachy.2017.08.010.

[60] H. Mizuno, T. Nakaji, S. Fukuda, and S. Kato, "End-to-end dosimetry audit for three-dimensional image-guided brachytherapy for cervical cancer," *Physica Medica*, vol. 119, Mar. 2024, doi: 10.1016/j.ejmp.2024.103321.

[61] J. Madamesila, P. McGeachy, J. E. Villarreal Barajas, and R. Khan, "Characterizing 3D printing in the fabrication of variable density phantoms for quality assurance of radiotherapy," *Physica Medica*, vol. 32, no. 1, pp. 242–247, Jan. 2016, doi: 10.1016/j.ejmp.2015.09.013.

[62] C. Lunsford, G. Grindle, B. Salatin, and B. E. Dicianno, "Innovations With 3-Dimensional Printing in Physical Medicine and Rehabilitation: A Review of the Literature," *PM and R*, vol. 8, no. 12, pp. 1201–1212, Dec. 2016, doi: 10.1016/J.PMRJ.2016.07.003.

[63] E. Ketels, "The role of 3D printing in radiotherapy," UHasselt & KU Leuven, Diepenbeek, 2024.

[64] V. Filippou and C. Tsoumpas, "Recent advances on the development of phantoms using 3D printing for imaging with CT, MRI, PET, SPECT, and ultrasound," *Med Phys*, vol. 45, no. 9, pp. e740–e760, Sep. 2018, doi: 10.1002/MP.13058,.

[65] B. P. Fahimian *et al.*, "3D printing in brachytherapy: A systematic review of gynecological applications," *Brachytherapy*, vol. 22, no. 4, pp. 446–460, Jul. 2023, doi: 10.1016/J.BRACHY.2023.02.002,.

[66] T. Chiu, Z. Xiong, D. Parsons, M. R. Folkert, P. M. Medin, and B. Hrycushko, “Low-cost 3D print–based phantom fabrication to facilitate interstitial prostate brachytherapy training program,” *Brachytherapy*, vol. 19, no. 6, pp. 800–811, Nov. 2020, doi: 10.1016/j.brachy.2020.06.015.

[67] J. Qiu *et al.*, “Constructing Customized Multimodal Phantoms Through 3D Printing: A Preliminary Evaluation,” *Front Phys*, vol. 9, Apr. 2021, doi: 10.3389/FPHY.2021.605630.

[68] A. L. Palmer, D. A. Bradley, and A. Nisbet, “Dosimetric audit in brachytherapy,” *Br J Radiol*, vol. 87, no. 1041, p. 20140105, Sep. 2014, doi: 10.1259/BJR.20140105.

[69] A. Dimitriadis *et al.*, “Development and international multicentre pilot testing of a postal dosimetry audit methodology for high dose rate brachytherapy,” *Phys Imaging Radiat Oncol*, vol. 32, Oct. 2024, doi: 10.1016/J.PHRO.2024.100665,.

[70] S. Gholami *et al.*, “A novel phantom design for brachytherapy quality assurance,” *Internatuinal Journal of Radiation Research*, vol. 14, no. 1, pp. 67–71, Jan. 2016, doi: 10.18869/ACADPUB.IJRR.14.1.67.

[71] A. Palmer, D. Bradley, and A. Nisbet, *Physics-aspects of dose accuracy in high dose rate (HDR) brachytherapy: Source dosimetry, treatment planning, equipment performance and in vivo verification techniques*, vol. 4, no. 2. 2012. doi: 10.5114/JCB.2012.29364.

[72] H. M. Linares Rosales, L. Archambault, S. Beddar, and L. Beaulieu, “Dosimetric performance of a multipoint plastic scintillator dosimeter as a tool for real-time source tracking in high dose rate 192Ir brachytherapy,” *Med Phys*, vol. 47, no. 9, pp. 4477–4490, Sep. 2020, doi: 10.1002/MP.14246,.

[73] L. Archambault, A. Sam Beddar, L. Gingras, R. Roy, and L. Beaulieu, “Measurement accuracy and Cerenkov removal for high performance, high spatial resolution scintillation dosimetry,” *Med Phys*, vol. 33, no. 1, pp. 128–135, 2006, doi: 10.1118/1.2138010,.

[74] H. M. Linares Rosales, L. Archambault, S. Beddar, and L. Beaulieu, “Dosimetric performance of a multipoint plastic scintillator dosimeter as a tool for real-time source tracking in high dose rate 192Ir brachytherapy,” *Med Phys*, vol. 47, no. 9, pp. 4477–4490, Sep. 2020, doi: 10.1002/MP.14246.

[75] J. Perez-Calatayud *et al.*, “Dose calculation for photon-emitting brachytherapy sources with average energy higher than 50 keV: Report of the AAPM and ESTRO,” May 2012. doi: 10.1118/1.3703892.

[76] D. E. Hyer, A. Sheybani, G. M. Jacobson, and Y. Kim, “The dosimetric impact of heterogeneity corrections in high-dose-rate 192Ir brachytherapy for cervical cancer: Investigation of both conventional Point-A and volume-optimized plans,” *Brachytherapy*, vol. 11, no. 6, pp. 515–520, Nov. 2012, doi: 10.1016/j.brachy.2012.01.011.

[77] L. Beaulieu *et al.*, “Report of the Task Group 186 on model-based dose calculation methods in brachytherapy beyond the TG-43 formalism: Current status and recommendations for clinical implementation,” John Wiley and Sons Ltd, Sep. 2012. doi: 10.1118/1.4747264.

[78] S. Devic, N. Tomic, and D. Lewis, “Reference radiochromic film dosimetry: Review of technical aspects,” *Physica Medica*, vol. 32, no. 4, pp. 541–556, Apr. 2016, doi: 10.1016/j.ejmp.2016.02.008.

[79] A. L. Palmer, A. Nisbet, and D. Bradley, “Verification of high dose rate brachytherapy dose distributions with EBT3 Gafchromic film quality control techniques,” *Phys Med Biol*, vol. 58, no. 3, pp. 497–511, Feb. 2013, doi: 10.1088/0031-9155/58/3/497,.

[80] J. Vanmol, “Experimental Evaluation of the HS-RP200 Optical Fiber Scintillator for Dosimetry in Clinical and Preclinical Radiotherapy,” UHasselt & KU Leuven, Diepenbeek, 2025.